American Mineralogist, Volume 97, pages 1749–1763, 2012

Second-order $P\bar{6}c2$-$P31c$ transition and structural crystallography of the cyclosilicate benitoite, $BaTiSi_3O_9$, at high pressure

Clivia Hejny,[1,*] Ronald Miletich,[2] Andreas Jasser,[3] Pascal Schouwink,[3,4] Wilson Crichton,[5] and Volker Kahlenberg[1]

[1]Institut für Mineralogie und Petrographie der Universität Innsbruck, Innrain 52, 6020 Innsbruck, Austria
[2]Institut für Mineralogie und Kristallographie der Universität Wien, Althanstrasse 14, 1090 Wein, Austria
[3]Institut für Geowissenschaften der Universität Heidelberg, Im Neuenheimer Feld 234, 69120 Heidelberg, Germany
[4]Laboratoire de Cristallographie de l'Université de Genève, 24, quai Ernest-Ansermet, 1211 Geneva 4, Switzerland
[5]European Synchrotron Radiation Facility, ESRF, 6 Rue Jules Horowitz, 38043 Grenoble, France

Abstract

Experimental high-pressure investigations on benitoite in the diamond-anvil cell reveal a second-order phase transition at a critical transition pressure $P_c = 4.24(3)$ GPa, as determined from synchrotron powder diffraction, single-crystal X-ray diffraction, and Raman spectroscopy. Diffraction experiments indicate a non-isomorphous transition from $P\bar{6}c2$ to $P31c$ space-group symmetry with $a' = a\sqrt{3}$ and $c' = c$ relative to the $P\bar{6}2c$ subcell below P_c. The high-pressure polymorph is characterized by a larger compressibility compared to the compressional behavior of benitoite below P_c. Fitting second-order Birch-Murnaghan equations of state to the experimental data sets, the parameters obtained are $V_0 = 372.34(4)$ Å^3, $K_0 = 117.9(7)$ GPa, with $a_0 = 6.6387(3)$ Å, $K_a = 108.1(7)$ GPa, and $c_0 = 9.7554(4)$ Å, $K_c = 143.3(1.1)$ GPa for the low-pressure form ($P < P_c$), and $V_0 = 376.1(4)$ Å^3, $K_0 = 88.9(1.6)$ GPa, with $a_0 = 11.516(4)$ Å, $K_a = 95.4(1.8)$ GPa, and $c_0 = 9.826(4)$ Å, $K_c = 77.2(1.6)$ GPa for the high-pressure form ($P > P_c$). One of the most significant structural changes is related to the coordination of Ba atoms, changing from an irregular [6+6] coordination to a more regular ninefold. Simultaneously, the Si_3O_9 rings are distorted due to no longer being constrained by mirror-plane symmetry, and the Si atoms occupy three independent sites. The higher compressibility along the **c**-axis direction is explained by the relative displacement of the Ba position to the Si_3O_9 rings, which is coupled to the lateral displacement of the non-bridging O2-type atoms of the ring unit. A symmetry mode analysis revealed that the transition is induced by the onset of a primary order parameter transforming according to the K_6 irreducible representation of $P\bar{6}c2$.

Keywords: Benitoite, crystal structure, phase transition, high pressure, diamond-anvil cell, X-ray diffraction, Raman spectroscopy, symmetry mode analysis

Introduction

The heterodesmic nature of complex silicate structures controls structural stability to a large extent, as well as properties and the behavior of a mineral subject to varying external variables such as pressure and temperature. Steric restrictions, as defined by the topology of the strongly bonded units, dictate the geometric flexibility of a structure. As a consequence of diverse and individual bonding, the majority of pressure-induced transitions in silicate minerals is determined by the degree of polymerization and the topological arrangement of quasi-rigid silicate subunits. On the other hand, units of finite polymerization (i.e., in chain-, ring-, and sheet-silicates) reveal additional degrees of freedom, as expressed by the less constrained rotation or tilting of finite building units. The effects of rotation, tilting, folding, and equivalent (or occasionally even competing) mechanisms are manifested by considerable anomalies in the elastic properties, i.e., showing deviations from linear elasticity behavior in particular when approaching the critical transition point of a structural instability (see e.g., Ullrich et al. 2009, 2010; Tröster et al. 2002; Carpenter and Salje 1998). Within the scope of scanning for high-pressure transitions with pronounced elastic-softening effects, silicate structures with three-membered (Si_nO_{3n})-ring units have been selected as potential candidates due to the rotational freedom of the ring units. Among several mineral structures, benitoite, $BaTiSi_3O_9$, has been in the focus of high-pressure crystallographic investigations due to the presence of the $(Si_3O_9)^{6-}$ silicate-ring units.

Although a quite rare mineral species, the cyclosilicate mineral has gained importance for the gemstone industry due to the well-developed euhedral crystal material occurring at the type localities in San Benito County and Fresno County, California (Louderback and Blasdale 1907, 1909; Louderback 1909, 1912; Alfors et al. 1965; Wise and Gill 1977). The structure of the hexagonal crystals (space group $P\bar{6}c2$), was solved early by Zachariasen (1930) and later confirmed by Fischer (1969). The exceptional point symmetry and hence the unusual [6+6]-fold coordination of barium atoms suggested a certain structural instability and also gave rise to speculations on the true space-group symmetry (Fischer 1969). Beyond these crystallographic studies structure-related investigations focused on trace-element

* E-mail: Clivia.Hejny@uibk.ac.at

0003-004X/12/0010–1749$05.00/DOI: http://dx.doi.org/10.2138/am.2012.4175

substitutions and the incorporation of hydrogen in natural crystals (Laird and Albee 1972; Beran 1974; Gaft et al. 2004). Within the mineralogical community benitoite is widely used in electron-microprobe laboratories as primary electron-microprobe standard due to its luminescence properties (Gaft et al. 2004, 2005; Takahashi et al. 2006), which are used for the alignment of the electron beam (Ma and Rossman 2008; Rossmann 2008).

There is a number of natural cyclosilicates known with one single type of a three-membered silicate ring, e.g., pabstite, $BaSnSi_3O_9$, and bazirite, $BaZrSi_3O_9$, both isostructural to benitoite (Hawthorne 1987). Wadeite, $K_2ZrSi_3O_9$ (Henshaw 1955; Blinov et al. 1977), and catapleiite, $Na_2ZrSi_3O_9 \cdot 2H_2O$ (Merlino et al. 2004; Zubkova et al. 2007), possess a similar heteropolyhedral framework topology of three-membered tetrahedral ring units, but different extra-framework cavities containing hydrated alkali atoms. Among numerous synthetic phases the tetragermanate and tetrasilicate structures of $BaGe(Si,Ge)_3O_9$ (Goreaud et al. 1973), $BaGeGe_3O_9$ (Robbins et al. 1966; Smolin 1969), $BaSiSi_3O_9$ (Finger et al. 1995; Hazen et al. 1999), $SrGeGe_3O_9$ (Nishi 1996), $PbGeGe_3O_9$ (Shashkov et al. 1981), and $Pb_{0.667}Sr_{0.333}GeGe_3O_9$ (Shashkov et al. 1984) have isolated three-membered rings incorporated into their structures, which are either strictly isostructural to benitoite or represent a topologically equivalent structure of reported lower (in all cases trigonal) symmetry.

Although the synthesis of tetragermanate and -silicate phases has been carried out at high-pressure conditions and, in addition, two different polymorphs have been reported for $BaGe_4O_9$ (Finger et al. 1995; Hazen et al. 1999), benitoite $BaTiSi_3O_9$, or any related analog silicate structure has not yet been subject to in situ structural investigations at high-pressure conditions. Here we report the results of in situ investigations on single crystals under hydrostatic conditions in the diamond-anvil cell, which comprise high-pressure X-ray diffraction techniques and vibrational spectroscopy to investigate the crystallography at high pressures. A principal objective of this study is to investigate the behavior of the structure at high pressures with particular focus on potential pressure-induced transformations, the character and mechanism of such a structural transformation, and the lattice elasticity of the polymorphs involved.

Materials and methods

Sample material

Experiments were carried out on oriented samples prepared from two centimeter-size pale-blue translucent natural crystals of gemstone quality from the type locality in San Benito, California. Two euhedral crystal fragments, provided from the collection of the "Institut für Geowissenschaften der Universität Heidelberg," were oriented by means of morphological faces and optical properties under crossed polarizers to give sections // (0001) and // $(11\bar{2}0)$ plane directions. The crystal orientation was validated by means of single-crystal X-ray diffraction. In addition to one-sided polished sections of the truncated crystals used for chemical investigations, double-sided polished oriented thin sections (35 μm thick for the crystal plate // **c**, 25 μm thick for the crystal cut ⊥ **c**) were prepared. All double-sided polished crystal sections were examined under crossed polarizers to check for twinning, mineral inclusions, and lattice imperfections. From the truncated part of the same crystal specimen a powdered sample was prepared for the synchrotron measurements. The composition of the sample crystals was investigated by energy-dispersive X-ray spectroscopy on a LEO 440 scanning electron microscope. Routine measurements were carried out with standard settings of operating conditions (tungsten filament, 20 kV acceleration power, 10 nA current) using a Peltier-cooled silicon-drift detector (Oxford Inca EDS System). Line-scan profiles across the sample reveal an ideal homogeneous composition without any indication of compositional heterogeneities. Moreover, the analyses show that contents of all elements other than Ba, Ti, and Si, in particular those of rare-earth elements, Sn, Zr, and Sr, are below the detection limit, which agrees well with the findings on chemical variations reported by Gaft et al. (2004). The analyses of a total of 25 individual data points yield on average 44.1(4) wt% SiO_2 [43.66–44.70%], 18.9(2) wt% TiO_2 [18.56–19.31%], and 37.0(3) wt% BaO [36.39–37.38%], from which the stoichiometric formula $Ba_{0.990(7)}Ti_{0.972(10)}Si_{3.017(24)}O_9$ was derived.

High-pressure sample loadings

High-pressure investigations were performed with opposed-anvil ETH-type (Miletich et al. 1999, 2000) diamond-anvil cells (DAC) using type *Ia* low-fluorescence diamond anvils with 600 μm culet-face diameter. Standard X-ray transparent beryllium backing plates (4 mm thickness) allowing for an opening angle of 90° were used for equation-of-state (EoS) measurements. For in situ Raman spectroscopy the optical port of the same backing plates provides an opening angle of 12°. For structural investigations the X-ray Bragg intensities were collected using a DAC with 2 mm thick single-crystal diamond backing plates (Miletich et al. 2000, 2005; Krauss et al. 2005; Periotto et al. 2011), which were manufactured with a conical double bevel cut (bevel angles 20° and 55°) from UP-7020 Sumicrystals.

All experiments were performed with stainless steel gaskets (steel type 1.4310) of 250 μm initial thickness that were pre-indented to 65–95 μm. The diameter of the mechanically drilled pressure chamber varied between 230 and 300 μm. For Raman microspectroscopy and for all XRD-measurements cryogenically liquefied argon and conventional water-free 4:1 methanol-ethanol mixtures were used as hydrostatic pressure media, respectively. Using spherical standard rubies (Chervin et al. 2002), pressures were derived from the spectral position of the laser-induced R_1 emission line ($^2E \rightarrow {}^4A_2$) of Cr^{3+} centers in the Al_2O_3 lattice to within an error of ~$1–2 \times 10^{-2}$ GPa by applying the empirical calibration parameters given by Mao et al. (1986) for hydrostatic conditions. For the EoS measurements accurate pressures were monitored to within 5×10^{-3} to 1.8×10^{-2} GPa by means of internal diffraction using the unit-cell volumes of the quartz calibrant (Angel et al. 1997). For in situ Raman microspectroscopy, two crystal fragments, corresponding to the two sections // (0001) and // $(11\bar{2}0)$, were loaded in argon together with several ruby spheres. Two different specimens in the orientation // $(11\bar{2}0)$ and measuring $230 \times 180 \times 35$ μm and $160 \times 120 \times 60$ μm in size, respectively, were loaded at any one time together with ruby in ethanol-methanol for single-crystal XRD investigations. A smaller crystal ($170 \times 75 \times 35$ μm) was used together with a calibrant quartz crystals ($105 \times 65 \times 50$ μm) in the loading prepared for the EoS measurements.

Synchrotron high-pressure powder-diffraction measurements

Synchrotron X-ray powder diffraction data were collected on samples pressurized between 0.97(2) and 9.50(2) GPa on an angle-dispersive setup in a stationary configuration (of ϕ) using a two-dimensional MAR345 image-plate detector system. All measurements were performed on the high-pressure beamline ID27 of the European Synchrotron Radiation Facility (ESRF), with a monochromatic beam of 33.2 keV ($\lambda = 0.3738$ Å), a spot size of about 6×10 μm, a sample-detector distance set to approximately 353 mm, and individual exposure times between 20 and 40 s. The setup was calibrated with a Si standard measured in the DAC. Debye diffraction rings were integrated with FIT2D (Hammersley et al. 1996) to give standard diffraction profiles. Rietveld refinements were carried out using the interface EXPGUI (Toby 2001) of the program GSAS (Larson and Von Dreele 2000). Along with the scale factor, lattice parameters *a* and *c*, mixing parameter ε as well as 5 profile parameters for a pseudo-Voigt peak profile were refined.

Equation of state measurements

High-precision measurements of the unit-cell parameters were performed at ambient conditions (294 K, 1 bar) and high pressures up to 8.60(2) GPa (Table 1) on a customized HUBER 5042 four-circle diffractometer, equipped with a type 512 Eulerian cradle, and a point detector with motorized slits parallel and perpendicular to the diffraction plane. Non-monochromatized Mo-radiation from a standard sealed-tube source, operated at 35 kV and 25 mA power settings, was used for the measurements of the Bragg intensities at the α_1,α_2-peak positions. The setting angles of diffracted Bragg peaks were recorded with a point detector, the slits of which were set to 2 and 9 mm, respectively, for scan directions within and perpendicular to the diffraction plane. Each reflection was centered in eight positions according to King and Finger (1979), so as to eliminate systematic aberrations for diffractometer settings and sample positioning. During the fitting of reflection

TABLE 1. Crystallographic unit-cell parameters as determined by single-crystal diffraction on two series of sample loadings (series A with 40 data points, series B with 3 data points)

no.	V(Qz) (Å^3)	P (GPa)	a (Å)	c (Å)	V (Å^3)	c/a
A-40	112.952(14)	10^{-4}	6.6403(7)	9.7542(6)	372.47(8)	1.46895(23)
A-39	111.896(9)	0.369(5)	6.6307(4)	9.7468(4)	371.12(5)	1.46995(14)
B-01	111.408(15)	0.543(8)	6.6279(6)	9.7450(6)	370.74(7)	1.47030(20)
A-38	111.085(17)	0.661(9)	6.6257(9)	9.7397(5)	370.29(9)	1.47999(26)
A-01	110.958(10)	0.708(6)	6.6240(4)	9.7389(4)	370.07(5)	1.47024(14)
B-02	110.944(9)	0.713(5)	6.6246(5)	9.7402(4)	370.19(5)	1.47030(15)
A-02	110.447(9)	0.901(5)	6.6198(5)	9.7350(6)	369.45(6)	1.47058(18)
A-37	110.023(9)	1.066(5)	6.6183(8)	9.7319(5)	369.16(9)	1.47047(24)
B-03	109.229(10)	1.387(6)	6.6096(11)	9.7229(15)	367.85(13)	1.47102(47)
A-36	107.031(12)	2.360(7)	6.5934(8)	9.7042(9)	365.35(9)	1.47182(29)
A-03	106.587(20)	2.574(11)	6.5888(4)	9.6992(4)	364.65(4)	1.47207(13)
A-04	106.549(10)	2.592(6)	6.5888(4)	9.6993(4)	364.65(4)	1.47207(12)
A-35	106.470(14)	2.631(8)	6.5874(4)	9.6955(5)	364.35(4)	1.47183(13)
A-05	106.443(10)	2.644(6)	6.5877(4)	9.6974(4)	364.46(5)	1.47205(14)
A-06	106.210(12)	2.759(7)	6.5842(4)	9.6945(5)	363.96(5)	1.47238(16)
A-34	106.130(15)	2.799(8)	6.5847(4)	9.6946(4)	364.02(4)	1.47229(13)
A-33	105.961(17)	2.884(9)	6.5830(5)	9.6925(5)	363.76(5)	1.47235(16)
A-07	105.745(14)	2.994(8)	6.5799(4)	9.6897(4)	363.31(4)	1.47261(13)
A-14	104.791(10)	3.497(6)	6.5725(5)	9.6817(5)	362.19(6)	1.47307(18)
A-32	104.735(17)	3.527(9)	6.5712(6)	9.6794(4)	361.96(7)	1.47300(23)
A-15	104.657(9)	3.570(5)	6.5710(7)	9.6796(7)	361.95(8)	1.47308(24)
A-16	104.419(9)	3.701(5)	6.5688(6)	9.6770(6)	361.61(7)	1.47317(22)
A-31	104.276(11)	3.780(6)	6.5666(11)	9.6730(8)	361.22(12)	1.47306(35)
A-17	104.186(12)	3.831(7)	6.5650(7)	9.6731(7)	361.05(8)	1.47345(25)
A-18	103.952(9)	3.964(5)	6.5623(8)	9.6707(8)	360.66(9)	1.47368(29)
A-30	103.638(14)	4.145(8)	6.5611(12)	9.6651(12)	360.32(14)	1.47310(46)
A-29	103.484(13)	4.235(7)	11.3609(16)	9.6620(10)	1080.00(30)	0.85045(21)
A-28	102.991(12)	4.529(7)	11.3517(16)	9.6519(11)	1077.12(29)	0.85026(21)
A-19	102.838(11)	4.623(6)	11.3439(11)	9.6478(9)	1075.18(22)	0.85048(15)
A-27	102.453(14)	4.860(8)	11.3429(23)	9.6456(15)	1074.75(45)	0.85037(30)
A-20	102.332(19)	4.936(10)	11.3362(17)	9.6419(10)	1073.07(35)	0.85054(22)
A-26	101.877(16)	5.227(9)	11.3330(38)	9.6293(26)	1071.06(78)	0.84967(53)
A-08	101.728(13)	5.324(7)	11.3247(7)	9.6296(5)	1069.52(14)	0.85032(9)
A-13	101.597(9)	5.410(5)	11.3218(6)	9.6275(4)	1068.74(11)	0.85034(7)
A-21	100.362(10)	6.256(6)	11.2928(13)	9.5966(12)	1059.86(28)	0.84980(20)
A-25	100.254(10)	6.333(6)	11.2908(23)	9.5918(19)	1058.96(46)	0.84952(34)
A-12	99.933(8)	6.565(5)	11.2836(5)	9.5907(6)	1057.51(16)	0.84996(11)
A-24	98.867(10)	7.369(6)	11.2632(13)	9.5640(11)	1050.75(27)	0.84914(20)
A-23	98.413(12)	7.728(7)	11.2520(19)	9.5528(12)	1047.42(41)	0.84899(27)
A-22	98.217(16)	7.886(9)	11.2446(19)	9.5472(11)	1045.43(36)	0.84904(24)
A-10	97.725(9)	8.291(5)	11.2305(8)	9.5373(6)	1041.71(16)	0.84923(11)
A-09	97.360(32)	8.600(18)	11.2219(8)	9.5269(5)	1038.99(14)	0.84895(10)

Note: Pressure values were derived from quartz unit-cell volumes after Angel et al. (1997).

profiles the α_1-α_2 peak splitting was treated by setting constraints on both the position and intensity ($\alpha_2/\alpha_1 = 0.53$) of the α_2-peak components as implemented in the SINGLE software (Angel and Finger 2011). The results of symmetry-constrained vector-least squares refinements are listed in Table 1.

Measurements of XRD Bragg intensities, structure solution, and refinements

In situ high-pressure X-ray intensity data were collected on an Oxford Diffraction Gemini three-circle diffractometer, equipped with a ruby CCD detector and using graphite-monochromatized Mo$K\alpha$ radiation (50 kV, 40 mA). Data collections were recorded at ambient conditions with the sample inside the DAC and at 1.12, 2.14, 3.56, 4.01, 4.28, 4.75, 5.29, and 6.14 ± 0.02 GPa. Data reduction includes intensity integration, background and Lorentz-polarization correction and were performed with the CrysAlis software package (Agilent Technologies 2011; CrysAlisPro Software system ver. 1.171.35.11.). The absorption correction for the crystal and effects of the high-pressure cell including the opening angle of the DAC, gasket shadowing and absorption by the diamond anvils was performed with the program ABSORB6.0 (Angel 2004); correction for diamond extinction dips were carried out with the program AVERAGE2.0 (Angel 2006). Empirical absorption corrections were carried out employing the total X-ray pathway $t = t_a + t_p$ through the diamond anvil (t_a) and diamond plate (t_p) and using an absorption coefficient $\mu_{dia} = 2.025$ cm^{-1}. The distance t_i was calculated from the incident/diffracted beam angle ψ_i ($\psi = 0$ to 45°), the bevel angles β_n and the bevel-culet distances d_n following the relationship $t_i = d_n/\cos(\psi_i-\beta_n)$, with $d_1 = 0.340$ cm and $\beta_1 = 0°$ for $0° \le \psi_i \le 23.8°$, $d_2 = 0.371$ cm and $\beta_2 = 20°$ for $23.8° \le \psi_i \le 39.5°$, and $d_3 = 0.379$ cm and $\beta_3 = 55°$ for $39.5° \le \psi_i \le 45°$.

The structure of the high-pressure form was solved from the data set measured at 4.75 GPa. A first attempt consisted in transforming the positional parameters of all positional parameters of the original benitoite structure to a setting corresponding to a unit cell with $a' = a\sqrt{3}$ and $c' = c$ and following the structure solutions in space group $P31c$ with the octahedral position on the origin as reported for the barium-tetragermanate and barium-tetrasilicate compounds (Smolin 1969; Goreaud et al. 1973; Hazen et al. 1999). All attempted refinements in this setting resulted in several negative thermal displacement parameters for individual atoms. Applying direct methods (by using the program SHELXS incorporated in the WINGX program suite Sheldrick 2008; Farrugia 1999) a structure solution in space group $P31c$ showed strong maxima on the threefold axis at the origin 0, 0, 0, and at 1/3, 2/3, $z \approx 0$, and 2/3, 1/3, $z \approx 0$, plus a strong maximum at ca. 1/3, 0, 0. Assigning the strongest maximum on the threefold axis to Ba, and the other to Ti, and adding up the Si and oxygen positions after consecutive difference Fourier calculations, the R-value finally converged to ~5%. Any attempt to refine data sets with this structural model transferred to the origin in the Ti positions resulted in unstable refinements. All intensity data were finally refined in the space groups $P\bar{6}2c$ (no. 188) and $P31c$ (no. 159) using the program JANA2006 (Petricek et al. 2006). Scattering curves for neutral atoms were taken from the *International Tables for X-ray Crystallography* volume C (Prince 2006). The final refinements were carried out with isotropic displacement parameters for all atoms. The experimental data are summarized in Table 2, the refined atomic coordinates and displacement parameters are given in Table 3, and the resulting interatomic bond distances are listed in Table 4. (The structural information has been deposited as CIF[1].)

Raman spectroscopy

Raman spectra were recorded in 180° backscattering geometry on a Jobin-Yvon HR800 confocal spectrometer equipped with an OLYMPUS BXFM-ILHS optical microscope, a grating with 1800 grooves per mm, and a Notch holographic filter, using a Peltier-cooled charge-coupled device (CCD) detector. The spectra were excited using the 632.82 nm line of a He-Ne laser operated at 20 mW. A 50× LWD (long working distance) objective (numerical aperture 0.70, free working distance ~10 mm) was used for laser beam focusing allowing a lateral resolution of ~2 µm and a spectral resolution of 0.8 cm^{-1}. The spectrometer was calibrated with neon lamp emissions and the silicon peak at 520.7 cm^{-1}, calibration spectra were collected for 1 s. The accumulation time for the ruby R luminescence lines was 3 s, while the benitoite Raman spectra were collected for 100–120 s per interval of 400 cm^{-1}. The wavenumber accuracy was higher than 0.5 cm^{-1}, and the spectral resolution was determined at ~2 cm^{-1}. Prior to the high-pressure experiment Raman modes of all samples were assigned for a range of 100–1200 cm^{-1} at 10^{-4} GPa, both mounted on one of the diamond anvils and on a glass slide. Fitting was done assuming pseudo-Voigt band shapes using the freeware FITYK 0.8.1 (Wojdyr 2010).

Symmetry mode analysis

The mathematical part of the mode decomposition was achieved by applying the computer program AMPLIMODES (Orobengoa et al. 2009) implemented only recently on the Bilbao Crystallographic Server. Using the input data corresponding to the structures at 10^{-4} and 4.75 GPa, in the first step a *reference structure* was calculated corresponding to the parent phase expressed in the setting of the low-symmetry phase (see Table 5). In the case of a polar structure (such as the high-pressure polymorph) the program automatically determines an origin shift along the polar direction to keep the arithmetric center of both phases. By means of this procedure some global shift of the polar compound due to the arbitrary choice of origin along the polar direction is eliminated. In our example, a shift of the origin parallel to **c** of 0.01709 (in relative units) was necessary. The resulting displacement field obtained from the comparison of the reference structure with the low-symmetry phase is given in Table 6. The displacement vectors **u** for the atoms in the asymmetric unit of the reference structure listed in this table completely define the displacive distortion relating both structures.

[1] Deposit item AM-12-074, CIF. Deposit items are available two ways: For a paper copy contact the Business Office of the Mineralogical Society of America (see inside front cover of recent issue) for price information. For an electronic copy visit the MSA web site at http://www.minsocam.org, go to the *American Mineralogist* Contents, find the table of contents for the specific volume/issue wanted, and then click on the deposit link there.

TABLE 2. Experimental details of the in situ high-pressure XRD intensity data collection and the structure refinements

Pressure (GPa)	0.0001	1.12(2)	2.14(1)	3.56(2)	4.01(2)	4.28(2)
Crystal size (μm)	160 × 120 × 60	160 × 120 × 60	160 × 120 × 60	160 × 120 × 60	160 × 120 × 60	160 × 120 × 60
Radiation	Mo*K*α	Mo*K*α	Mo*K*α	Mo*K*α	Mo*K*α	Mo*K*α
a (Å)	6.6430(6)	6.6094(4)	6.6031(11)	6.5689(4)	6.5605(6)	6.5518(8)
c (Å)	9.7660(14)	9.7239(7)	9.710(2)	9.6804(7)	9.6574(11)	9.6503(16)
V (Å^3)	373.23(15)	367.87(12)	366.65(19)	361.7(2)	359.97(13)	358.75(15)
Z	2	2	2	2	2	2
V/*Z* (Å^3)	186.62	183.94	183.33	180.85	179.99	179.38
2θ range (°)	2–58	2–58	2–58	2–58	2–58	2–58
Scan type	ω	ω	ω	ω	ω	ω
Scan speed (°/s)*	0.033 (30 s)	0.033 (30 s)	0.154 (6.25 s)	0.183 (5.45 s)	0.157 (6.38 s)	0.183 (5.45)
Scan width (°)	1.0	1.0	1.0	1.0	1.0	1.0
Detector-sample distance (mm)	83	83	83	83	83	83
Space group	*P*$\bar{6}$*c*2 (no. 188)	*P*$\bar{6}$*c*2 (no. 188)	*P*$\bar{6}$*c*2 (no. 188)	*P*$\bar{6}$*c*2 (no. 188)	*P*$\bar{6}$*c*2 (no. 188)	*P*$\bar{6}$*c*2 (no. 188)
Reflections measured	3538	3004	2801	2990	2476	2549
Unique reflections (total)	158	165	157	167	155	157
Unique reflections $F_o > 3\sigma(F_o)$	135	134	120	135	120	127
Parameters refined	13	13	13	13	13	13
R_{int}	0.065	0.078	0.098	0.075	0.073	0.071
$R_1(F)$ obs/all	0.0382/0.0404	0.0391/0.0439	0.0378/0.0420	0.0493/0.0595	0.0447/0.0570	0.0559/0.0638
GooF	1.22	0.93	0.79	1.18	1.18	1.52

Pressure (GPa)	4.75(2)	5.29(2)	6.14(2)
Crystal size (μm)	160 × 120 × 60	230 × 180 × 35	230 × 180 × 35
Radiation	Mo*K*α	Mo*K*α	Mo*K*α
a (Å)	11.3382(9)	11.3177(10)	11.2984(10)
c (Å)	9.6584(9)	9.6293(10)	9.6051(12)
V (Å^3)	1075.3(3)	1068.2(4)	1061.9(3)
Z	6	6	6
V/*Z* (Å^3)	179.22	178.03	176.98
2θ range (°)	2–58	2–58	2–58
Scan type	ω	ω	ω
Scan speed (°/s)*	0.033 (30.6 s)	0. 033 (30 s)	0.0227 (44 s)
Scan width (°)	1.0	1.0	1.0
Detector-sample distance (mm)	83	83	83
Space group	*P*31*c* (no. 159)	*P*31*c* (no. 159)	*P*31*c* (no. 159)
Reflections measured	8682	5193	4285
Unique reflections (total)	705	686	676
Unique reflections $F_o > 3\sigma(F_o)$	346	376	327
Parameters refined	58	58	58
R_{int}	0.067	0.062	0.086
$R_1(F)$ obs/all	0.0480/0.0758	0.0418/0.0621	0.0470/0.0702
GooF	1.13	1.05	1.04

* Value in parentheses: time per frame.

RESULTS

Diffraction pattern and X-ray crystallography

The synchrotron powder diffraction data collected at ESRF revealed high-quality diffraction images indicating ideal hydrostatic conditions (see Fig. 1). Careful inspection of diffraction rings by comparison of the patterns at different pressures reveals additional reflections appearing above ~4.3 GPa, which do not match the unit-cell parameters of benitoite as extrapolated to the given pressure. Attempts to index the new lines based on the original benitoite unit cell reveal *hkl* indices with *h,k* = (3n + 1)/3 and (3n + 2)/3. It is possible to index these reflections with conventional integer Miller indices by transforming the *a*-axis to a hexagonal setting via the relationship $a' = a\sqrt{3}$. Moreover, the additional lines observed in the patterns at 5.23, 5.71, 7.65, and 9.50 GPa appear to increase in relative intensity on increasing pressure.

Sections through the reciprocal space reconstructed from the frames recorded for XRD structure evaluation provide a similar picture for all measurements at pressures higher than ~4.3 GPa (Fig. 2) and confirm the transformation to a setting with $a' = a\sqrt{3}$, and $c' = c$. Isomorphic subgroups of *P*$\bar{6}$*c*2 are *P*3*c*1, *P*312, and *P*3, but according to the relationship $\mathbf{a}'^* = \mathbf{a}_1^*/3 + \mathbf{a}_2^*/3$ in reciprocal space, possible direct subgroups are *P*31*c*, *P*321, and *P*3. Since reflections with $l = 2n + 1$ for *hhl* are absent, which indicates the presence of a *c*-glide plane, *P*31*c* was assumed to be the correct space group of the new high-pressure structure with $a' = a\sqrt{3}$ and $c' = c$ relative to the benitoite *P*$\bar{6}$2*c* subcell.

A similar unit-cell setting has been reported previously on several synthetic analog phases such as $BaGeGe_3O_9$ (Robbins et al. 1966; Smolin 1969), $BaGe(Si,Ge)_3O_9$ (Goreaud et al. 1973), and $BaSiSi_3O_9$ (Hazen et al. 1999). Although a lower space-group symmetry (*P*3, *P*31c, or *P*321) was reported, their structures were found to correspond to the benitoite archetype structure, however with displacements of the atoms away from special positions (Finger et al. 1995; Hazen et al. 1999; Finger and Hazen 2000). Moreover, $BaSiSi_3O_9$, (Hazen et al. 1999) was reported to transform upon grinding into the benitoite structure (Finger et al. 1995; Finger and Hazen 2000), indicating a mechanically induced transformation.

Static compression and equation of state

Lattice dimensions and unit-cell volumes derived from single-crystal X-ray diffraction are plotted in Figure 3. Both the volume

TABLE 3. Refined atomic positions and isotropic displacement parameters (Å^2) for benitoite $BaTiSi_3O_9$ and its high-pressure polymorph

Site	*P* (GPa)	x/a	y/b	z/c	U_{iso}	Site	*P* (GPa)	x/a	y/b	z/c	U_{iso}
Ba	0.0001	0.6667	0.3333	0	0.0074(5)	Ti	4.75	0.333(1)	0.999(2)	0.0181(7)	0.005(1)
	1.12	0.6667	0.3333	0	0.0164(5)		5.29	0.3332(3)	0.9993(3)	0.0265(5)	0.0040(9
	2.14	0.6667	0.3333	0	0.0090(5)		6.14	0.3326(3)	0.9989(3)	0.0321(6)	0.0068(11)
	3.56	0.6667	0.3333	0	0.0087(6)	Si1	4.75	0.717(1)	0.881(2)	0.2631(1)	0.005(2)
	4.01	0.6667	0.3333	0	0.0079(7)		5.29	0.7168(5)	0.8803(5)	0.2673(7)	0.0052(11)
	4.28	0.6667	0.3333	0	0.0086(8)		6.14	0.7166(6)	0.8800(6)	0.2702(8)	0.0075(13)
Ti	0.0001	0.3333	0.6667	0	0.0032(15)	Si2	4.75	0.170(1)	0.787(2)	0.770(1)	0.002(2)
	1.12	0.3333	0.6667	0	0.0114(14)		5.29	0.1713(5)	0.7885(5)	0.7783(7)	0.0006(9)
	2.14	0.3333	0.6667	0	0.0040(15)		6.14	0.1718(5)	0.7883(6)	0.7845(8)	0.0065(11)
	3.56	0.3333	0.6667	0	0.0024(17)	Si3	4.75	0.497(1)	0.949(1)	0.271(1)	0.003(2)
	4.01	0.3333	0.6667	0	0.002(2)		5.29	0.4980(5)	0.9501(5)	0.2805(7)	0.0013(10)
	4.28	0.3333	0.6667	0	0.002(2)		6.14	0.4969(6)	0.9508(6)	0.2862(9)	0.0084(12)
Si	0.0001	0.0705(8)	0.7817(8)	0.25	0.0014(10)	O11	4.75	0.044(2)	0.817(2)	0.774(2)	0.003(4)
	1.12	0.0707(8)	0.7821(8)	0.25	0.0094(9)		5.29	0.0428(12)	0.8168(12)	0.7847(14)	0.003(4)
	2.14	0.0698(8)	0.7814(8)	0.25	0.0022(10)		6.14	0.0429(13)	0.8151(13)	0.7919(16)	0.004(3)
	3.56	0.0687(10)	0.7803(9)	0.25	0.0015(11)	O12	4.75	0.625(4)	0.106(3)	0.266(2)	0.006(4)
	4.01	0.0688(12)	0.7806(12)	0.25	0.0004(15)		5.29	0.6213(13)	0.1059(13)	0.2736(15)	0.011(3)
	4.28	0.0687(13)	0.7813(13)	0.25	0.0018(16)		6.14	0.6209(16)	0.1054(15)	0.2773(18)	0.019(4)
O1	0.0001	0.809(2)	0.745(2)	0.25	0.0024(13)	O13	4.75	0.563(3)	0.851(3)	0.260(2)	0.010(3)
	1.12	0.810(2)	0.746(2)	0.25	0.010(3)		5.29	0.5594(11)	0.8473(12)	0.2660(14)	0.003(3)
	2.14	0.809(2)	0.747(2)	0.25	0.002(3)		6.14	0.5595(14)	0.8484(15)	0.2663(17)	0.013(4)
	3.56	0.808(3)	0.743(2)	0.25	0.002(3)	O21	4.75	0.758(2)	0.835(2)	0.122(2)	0.007(4)
	4.01	0.812(3)	0.745(3)	0.25	0.001(4)		5.29	0.7601(12)	0.8404(12)	0.1253(13)	0.007(3)
	4.28	0.811(3)	0.745(3)	0.25	0.001(4)		6.14	0.7628(15)	0.8439(15)	0.1293(18)	0.017(3)
O2	0.0001	0.0862(14)	0.6578(16)	0.3877(8)	0.0039(17)	O22	4.75	0.415(2)	0.160(2)	0.133(2)	0.005(4)
	1.12	0.0861(14)	0.6555(15)	0.3878(8)	0.0118(16)		5.29	0.4097(12)	0.1584(11)	0.1370(14)	0.004(3)
	2.14	0.0867(14)	0.6568(16)	0.3881(8)	0.0047(16)		6.14	0.4084(13)	0.1562(13)	0.1436(16)	0.006(3)
	3.56	0.0851(16)	0.6533(18)	0.3874(8)	0.0031(19)	O23	4.75	0.402(2)	0.911(2)	0.137(2)	0.003(4)
	4.01	0.087(2)	0.653(2)	0.3877(13)	0.002(2)		5.29	0.3969(11)	0.9099(11)	0.1456(13)	0.003(5)
	4.28	0.086(2)	0.653(2)	0.3882(14)	0.001(3)		6.14	0.3931(13)	0.9088(13)	0.1585(15)	0.009(3)
Ba1	4.75	0	0	0	0.010(2)	O21m	4.75	0.821(2)	0.749(2)	0.897(2)	0.005(4)
	5.29	0	0	0	0.0043(6)		5.29	0.8198(12)	0.7478(12)	0.9018(13)	0.004(3)
	6.14	0	0	0	0.0081(7)		6.14	0.8165(14)	0.7464(14)	0.9035(16)	0.009(3)
Ba2	4.75	0.66667	0.33333	0.026(1)	0.009(3)	O22m	4.75	0.262(2)	0.836(2)	0.907(2)	0.008(4)
	5.29	0.6667	0.3333	0.0370(3)	0.0094(6)		5.29	0.2592(13)	0.8346(13)	0.9175(14)	0.011(3)
	6.14	0.6667	0.3333	0.0460(4)	0.0147(7)		6.14	0.2662(14)	0.8369(15)	0.9189(17)	0.012(3)
Ba3	4.75	0.33333	0.66667	0.027(1)	0.00981	O23m	4.75	0.500(2)	0.086(2)	0.913(2)	0.004(4)
	5.29	0.3333	0.6667	0.0375(3)	0.0092(6)		5.29	0.5037(11)	0.0875(11)	0.9240(12)	0.002(5)
	6.14	0.3333	0.6667	0.0463(4)	0.0141(7)		6.14	0.5044(14)	0.0890(14)	0.9331(16)	0.008(3)

data and the individual crystallographic axis do not indicate any discontinuity, which would have been a fingerprint of a classical first-order phase transition. Careful inspection reveals that, at the critical pressure, between approximately 4 and 4.5 GPa, the evolution of the **c**-axis, and consequently the volume data, do not follow the conventional compression behavior. The **c**-axis starts getting softer while crossing the critical transition point. The apparent compressibility of the **c**-axis is clearly higher for the high-pressure polymorph, while the compression of the **a**-axis appears not to get changed in a significant manner. This is also confirmed by the evolution of the *c*/*a* ratio with pressure (Fig. 4), which reveals increasing values up to a maximum between ~4 and 4.5 GPa, and a decrease of *c*/*a* beyond the transition point.

The evaluation of the compressibilites by fitting the conventional EoS parameters according to a Birch-Murnaghan (BM) formalisms to the experimental data (cf. Angel 2000) requires little effort for the analysis. The *F-f* plot (Fig. 5a) reveals straight lines with almost no slope, suggesting that the value of the pressure derivative K_0' (=dK/dP) of the bulk modulus K_0 must be close to 4. Any attempt to fit the two sets of truncated data to a conventional third-order BM EoS yielded insignificant values with large uncertainties for K_0' and the corresponding correlation with K_0 and V_0. Accordingly, all fits were carried out with truncations of the BM equation at second order, i.e., fixing K_0' to a value of 4 as implied by the results from finite strain analysis. Moreover, various attempts were made with omitting individual data points in the proximity of the critical transition. Finally, the fits were performed with the data points $P \leq 4.145$ GPa for the low-pressure polymorph (LPP), and with $P \geq 4.623$ GPa for the high-*P* polymorph (HPP). The resulting values (Table 7) confirm the findings that the HPP has a higher compressibility than the LPP. This is confirmed not only by the volume, but also for the compression along the crystallographic **a** and **c** axis directions.

Comparing these two main directions, the softening of the **c**-axis is pronounced by a reduction from K_c(LPP) = 143.4 GPa to K_c(HPP) = 77.2 GPa, while the effect on the **a**-axis direction is much less distinct [K_a(LPP) = 108.1 GPa, K_a(HPP) = 95.4 GPa]. Calculating the spontaneous strain (Fig. 5b), which arises from the differences relative to the extrapolated values of the volume and individual axes, the pronounced difference between the two axes is obvious. Moreover, the evolution of the strain follows a linear fashion, which suggests the transition to be second order in character, as e_{ij} scales linearly with $(P_c - P)$ according to the relations between the strain component, order parameter and pressure, i.e., $e_{ij} \propto Q^2$ and $Q \propto (P_c - P)^{1/2}$. Fitting straight lines to the e_{33} and e_v strain components, the intercepts at $e = 0$ suggest a transition pressure to lie between 4.15(46) and 4.20(33) GPa, which is in perfect agreement with the value of 4.243(22) GPa as derived from the mathematical intersect between the fitted *P-V*, *P-a*, and *P-c* equations of the HPP and the LPP forms.

TABLE 4. Bond distances (Å) and selected angles (°) for benitoite $BaTiSi_3O_9$ and its high-pressure polymorph

	Fischer et al. (1969)	10^{-4} GPa	1.12 GPa	2.14 GPa	3.56 GPa	4.01 GPa	4.28 GPa
Ba-O2 (6×)	2.767(2)	2.758(7)	2.740(7)	2.740(7)	2.717(11)	2.710(11)	2.710(15)
Ba-O1 (6×)	3.434	3.429(9)	3.414(9)	3.417(9)	3.385(9)	3.385(11)	3.380(12)
Ti-O2 (6×)	1.942(2)	1.950(1)	1.935(8)	1.931(13)	1.927(11)	1.913(14)	1.913(15)
Si-O1	1.630(3)	1.632(16)	1.614(16)	1.622(16)	1.603(19)	1.583(22)	1.583(23)
Si-O1	1.648(3)	1.646(15)	1.640(16)	1.628(15)	1.649(18)	1.644(17)	1.641(17)
Si-O2	1.605(2)	1.608(10)	1.610(10)	1.606(10)	1.602(11)	1.606(15)	1.608(15)
<Si-O>	1.622	1.624	1.619	1.616	1.614	1.610	1.610
O1-Si-O1	107.1(1)	107.5(9)	107.1(9)	107.0(8)	108.2(10)	107.2(12)	107.7(14)
Si-O1-Si	132.9(1)	132.5(7)	132.9 (7)	133.0(7)	131.8(8)	132.8(10)	132.3(11)

	4.75 GPa	5.29 GPa	6.14 GPa
Ba1-O21 (3×)	2.685(13)	2.681(19)	2.669(16)
Ba1-O21m (3×)	2.728(11)	2.716(10)	2.725(15)
Ba1-O11 (3×)	3.205(17)	3.136(15)	3.099(17)
Ba1-O11 (3×)	3.543(16)	3.613(15)	3.667(17)
<Ba1-O>*	2.873	2.844	2.831
Ba2-O22 (3×)	2.711(13)	2.747(11)	2.748(15)
Ba2-O23m (3×)	2.690(12)	2.682(11)	2.666(16)
Ba2-O12 (3×)	3.337(15)	3.280(15)	3.240(18)
Ba2-O13 (3×)	3.496(17)	3.508(12)	3.559(15)
<Ba1-O>*	2.913	2.903	2.885
Ba3-O23 (3×)	2.676(15)	2.683(11)	2.693(18)
Ba3-O22m (3×)	2.700(18)	2.693(16)	2.695(16)
Ba3-O13 (3×)	3.260(14)	3.214(11)	3.158(17)
Ba3-O12 (3×)	3.479(15)	3.468(15)	3.494(18)
<Ba1-O>*	2.879	2.863	2.849
Ti-O21	1.931(16)	1.951(13)	1.951(13)
Ti-O22	1.934(14)	1.888(12)	1.888(12)
Ti-O23	1.952(18)	1.894(15)	1.894(15)
Ti-O21m	1.880(19)	1.927(18)	1.927(18)
Ti-O22m	1.941(16)	1.928(14)	1.928(14)
Ti-O23m	1.928(14)	1.941(12)	1.941(12)
<Ti-O>	1.928	1.921	1.922
Si1-O11	1.598(14)	1.619(12)	1.615(12)
Si1-O13	1.671(19)	1.630(15)	1.627(15)
Si1-O21	1.612(18)	1.594(15)	1.593(16)
Si1-O21m	1.619(17)	1.581(15)	1.584(15)
<Si1-O>	1.625	1.606	1.605
O11-Si1-O13	107.6(10)	108.9(8)	109.0(8)
Si1-O11-Si1	131.2(11)	132.0(9)	131.9(9)
Si2-O11	1.64(2)	1.651(17)	1.640(17)
Si2-O12	1.628(15)	1.649(13)	1.653(13)
Si2-O22	1.583(16)	1.580(15)	1.577(15)
Si2-O22m	1.595(17)	1.596(14)	1.593(15)
<Si2-O>	1.612	1.619	1.616
O11-Si2-O12	107.2(8)	106.9(7)	107.0(7)
Si3-O12-Si2	134.0(13)	131.3(11)	131.3(11)
Si3-O12	1.588(12)	1.603(11)	1.613(11)
Si3-O13	1.59(2)	1.631(18)	1.632(17)
Si3-O23	1.594(15)	1.642(14)	1.638(14)
Si3-O23m	1.609(17)	1.601(15)	1.599(15)
<Si3-O>	1.595	1.619	1.621
O12-Si3-O13	106.9(9)	110.0(7)	109.4(8)
Si1-O13-Si3	132.3(9)	130.0(7)	129.8(7)
γ† to O21-O21m	3.1 (5)	3.9(4)	5.0 (5)
γ† to O22-O22m	3.8 (5)	5.7(5)	7.8 (6)
γ† to O23-O23m	1.8 (6)	3.0(4)	3.6 (6)
Γ†	1.7(2)	2.6(2)	3.3(2)

* <Ba-O> calculated from 9 Ba-O distances up to a maximum Ba-O distance of 3.34 Å.
† For definition of tilt angle γ and Γ see text and Figure 10.

TABLE 5. Calculated reference structure for low-pressure (high-symmetry) benitoite in space group *P*31*c* (*a* = *b* = 11.4478 Å, *c* = 9.7239 Å)

Atom	Wyckoff site	x	y	z
Ba1	2*a*	0.000000	0.000000	0.500000
Ba2	2*b*	0.666667	0.333333	0.500000
Ba3	2*b*	0.333334	0.666667	0.500000
Ti1	6*c*	0.666667	0.666667	0.500000
Si1	6*c*	0.715733	0.880234	0.250000
Si2	6*c*	0.786433	0.168834	0.250000
Si3	6*c*	0.497833	0.950934	0.250000
O11	6*c*	0.227333	0.185334	0.250000
O12	6*c*	0.481333	0.375334	0.250000
O13	6*c*	0.291333	0.439334	0.250000
O21	6*c*	0.752800	0.827767	0.112200
O22	6*c*	0.838900	0.258367	0.112200
O23	6*c*	0.408300	0.913867	0.112200
O21m	6*c*	0.752800	0.827767	0.387800
O22m	6*c*	0.838900	0.258367	0.387800
O23m	6*c*	0.408300	0.913867	0.387800

TABLE 6. Displacement field for the high-pressure phase after the origin shift

Atom site	Wyckoff	u_x	u_y	u_z	|u|
Ba1	2*b*	0.0000	0.0000	–0.0171	0.1662
Ba2	2*a*	0.0000	0.0000	0.0091	0.0886
Ba3	2*b*	–0.0000	0.0000	0.0090	0.0876
Ti1	6*c*	0.0006	0.0004	–0.0004	0.0074
Si1	6*c*	0.0024	0.0016	–0.0052	0.0558
Si2	6*c*	–0.0004	0.0001	0.0021	0.0212
Si3	6*c*	–0.0012	–0.0000	0.0032	0.0342
O11	6*c*	–0.0019	–0.0025	0.0073	0.0758
O12	6*c*	–0.0000	0.0036	–0.0013	0.0429
O13	6*c*	0.0030	0.0024	–0.0081	0.0846
O21	6*c*	0.0076	0.0060	–0.0068	0.1034
O22	6*c*	–0.0008	–0.0043	0.0012	0.0465
O23	6*c*	–0.0058	–0.0043	0.0066	0.0877
O21m	6*c*	–0.0030	–0.0100	–0.0078	0.1265
O22m	6*c*	–0.0028	0.0031	0.0000	0.0589
O23m	6*c*	0.0047	–0.0016	0.0087	0.1066

Notes: u_x, u_y, and u_z are given in relative units. |u| is the absolute displacement in angstroms.

Structures of the polymorphs and their high-pressure behavior

The original benitoite structure was solved by Zachariasen (1930) and later confirmed by Fischer (1969). The crystal structure (Fig. 6) can be described by a layered corner-linked framework, which is composed by alternating three-membered (Si_3O_9) rings and isolated TiO_6 octahedra. Barium atoms occupy a central position in large structural channels within this framework. Within the rings each SiO_4 tetrahedron shares two of its oxygen atoms, the bridging atoms O1, with adjacent tetrahedra. The ring symmetry is $\bar{6}$ with Si and O1 being located on the mirror plane, and the Si_3O_9 rings are arranged in layers perpendicular to the **c** axis. Stacked along the **c**-axis direction, the rings are rotated within the (0001) plane by ~33° against each other. Both the barium and titanium atoms occupy special positions on the triads parallel to the **c**-axis and occupy sites of the point symmetry (3.2). The Ti atoms (Wyckoff site 2*c*) are octahedrally coordinated to the oxygen atoms, being corner-linked with the Si_3O_9 rings by sharing one of their non-bridging oxygen atoms. The Ba atoms (Wyckoff site 2*e*) show an unusual [6+6]-fold

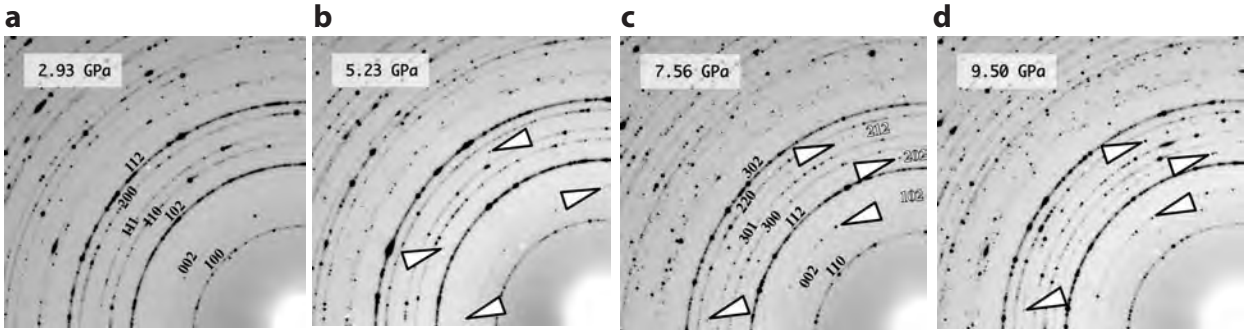

FIGURE 1. Detail sections of the X-ray diffraction pattern recorded at 2.93, 5.23, 7.56, and 9.50 GPa. Additional Debye rings (white arrows) corresponding to the supercell arise at pressures above 4.3 GPa and gain intensity with increasing pressure. Line indexing changes from the subcell with a and c to the supercell with with $a' = a\sqrt{3}$ and $c' = c$.

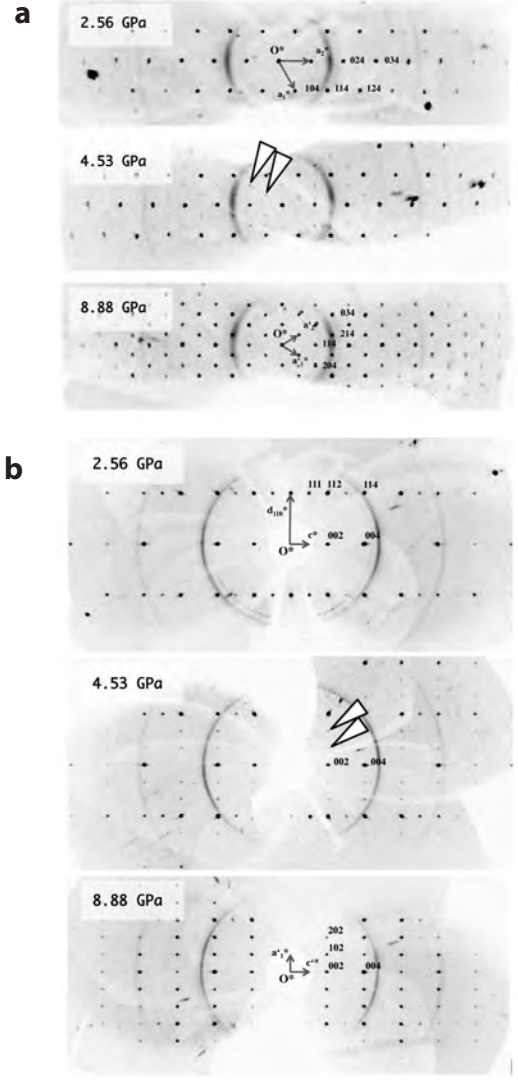

FIGURE 2. Two-dimensional sections through the reconstructed accessible reciprocal space in (**a**) *hk*4 and (**b**) *hhl* plane direction. The images above 4.3 GPa reveal the superstructure reflections (white arrows) corresponding to the supercell with $a' = a\sqrt{3}$ and $c' = c$. Reconstructions were performed from individual frames using CrysAlis software (Agilent Technologies 2001; CrysAlisPro Software system 1.171.35.11.).

coordination with Ba-O distances of 2.77 and 3.43 Å, which exhibits a highly symmetric 12-fold coordinated polyhedron with exceptionally high bond-length distortion. Considering only the 6 short bonds to belong to the coordination sphere, as suggested by Zachariasen (1930) and Fischer (1969) and that also follows Pauling's principles, the coordination resembles a highly distorted octahedron.

Examining the structure above the transition, the symmetry breaking from $P\bar{6}c2$ to $P31c$ leads to a splitting of the single Ba site into three sites (Ba1, Ba2, Ba3), each of them lying onto a triad (point symmetry 3) occupying the Wyckoff positions 2*a* (0,0,*z*) and 2*b* (1/3, 2/3, *z*; 2/3, 1/3, *z*). The Ti site remains a unique one, but changes from a special position (point symmetry 32) to that of the general position (Wyckoff site 6*c*, point symmetry 1) with $x \approx 1/3$ and $y \approx 0$. All three Si atoms (Si1, Si2, Si3) and oxygen atoms (O11, O12, O13, O21, O22, O23, O21m, O22m, O23m) are also located on general positions. The *z* coordinates of the atoms generated from the Si and O1 atoms are close to 0.25 and 0.75, which corresponds to position of the former *m* plane || (001), and deviate increasingly from these values with increasing pressure (Fig. 7). The stronger deviation of Si2 and Si3 in comparison to Si1 can be explained by their connection via the terminal oxygen atoms O22 and O22m to Ba2 and via O23 and O23m to Ba3, respectively. Ba2 and Ba3 display a similar increasing deviation from their position of $z = 0$ in the LPP, whereas the position of Ba1 has been fixed to $z = 0$.

The most dramatic changes related to the structural transformation at 4.3 GPa is the change in the coordination of the Ba atoms, which changes from sixfold to ninefold (Fig. 8). As being no more constrained by symmetry three of the nonbonding Ba-O1 distances of the LPP phase are getting significantly shortened from ~3.4 Å in the LPP to distances between 3.10 and 3.24 Å at 6.14 GPa, while the remaining three Ba-O1 distances increase to Ba-O1*i* (*i* = 1,2,3) values of 3.50 to 3.67 Å (Figs. 8 and 9). Simultaneously a small shift of the Ba atoms along the *z* direction toward the subset of O2*i* (*i* = 1,2,3) atoms leads to shortening of these three Ba*i*-O2*i* distances, while the remaining Ba*i*-O2*i*m distances increase. The diversification of these short Ba-O bonds is also supported by shifts of the oxygen atoms, which lead to internal distortion of the Si_3O_9 rings, as the O2 atoms are shared between Ba and Si atoms.

Contrary to the obvious changes on the barium stereochem-

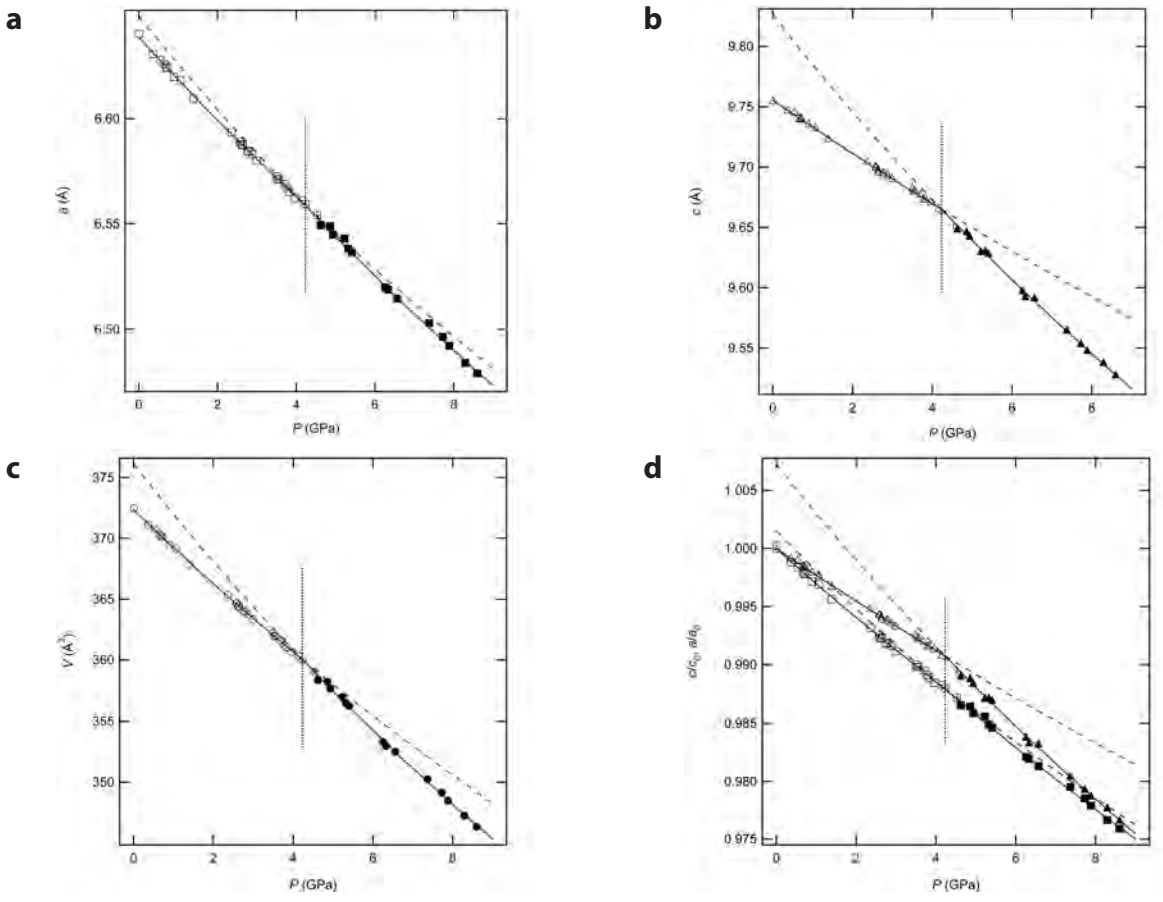

FIGURE 3. Evolution of the unit-cell dimensions a, c, V, and the calculated relative parameters a/a_0 and c/c_0 as a function of pressure. Individual data points correspond to the values obtained by single-crystal diffraction and listed in Table 1. The plotted values related to the a-axis of the high-pressure form are given as $a/\sqrt{3}$ corresponding to low-pressure subcell parameter. Errors for the measured parameter and pressure are smaller than the given symbol size. The lines correspond to the fits represented in Table 7. The vertical line indicates the critical transition pressure at 4.23 GPa.

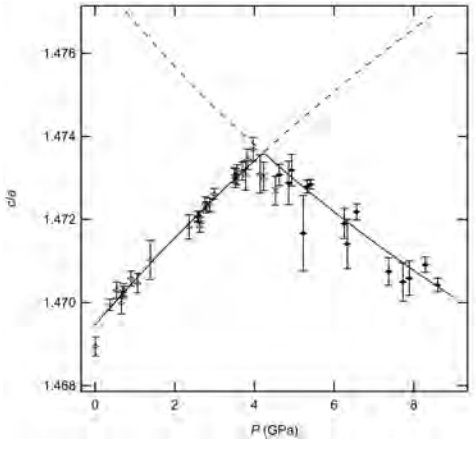

FIGURE 4. Calculated c/a ratio as a function of pressure. The values above the critical transition point P_c were calculated accounting for the relationship $a'_{HPP} = a_{LPP}\sqrt{3}$ as $c\sqrt{3}/a$ corresponding to a c/a ratio equivalent to the low-pressure subcell. The lines plotted in the graph represent the arithmetical c/a ratio as derived from the second-order Birch-Murnaghan equations for the a and c axes corresponding to the fit parameters given in Table 7.

istry, both the Ti and Si atoms show almost no difference apart from symmetry aspects. The octahedral coordination of the Ti atoms is very regular with only small variations for individual Ti-O bond distances (ranging between 1.88 and 1.96 Å). Considering the mean distances and the non-existing trends of variations with pressure, the variations of Si-O distances with pressure are in a similar fashion also not of considerable significance. Nevertheless, the relative positional displacements of the oxygen atoms reveal some distinct internal polyhedral distortion and tilting of tetrahedra within the (Si1Si2Si3)O_9 ring unit. In the HPP structure the three-membered ring of tetrahedra is not on the threefold axis anymore and also loses its mirror-plane symmetry, so that Si and O1x atoms connecting the silicon tetrahedra within the ring are not constrained on the ring plane anymore. One of the most noticeable characteristics is the inclination of the O2*i*-O2*i*m edge of the SiO_4 tetrahedra (Fig. 10). Due to the mirror-plane symmetry in $P\bar{6}c2$, the corresponding O2-O2′ is exactly parallel to the **c**-axis direction, while in $P31c$ the corresponding tetrahedron edge tilts relative to the ring plane. Kahlenberg et al. (2007) have defined the angle γ as the angle between the terminal oxygen atoms of each tetrahedron (O2-O2 in the LPP and O2*i*-O2*i*m in the HPP) and

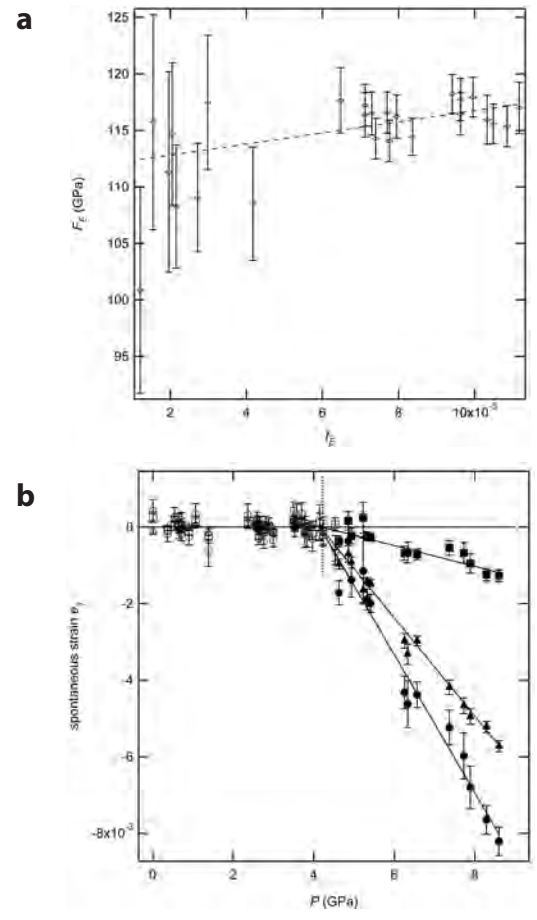

FIGURE 5. (**a**) Normalized pressure F_E vs. Eulerian strain f_E calculated for the pressure–volume data of the LPP phase. (**b**) Variation of the individual components of spontaneous strain arising due to the $P\bar{6}c2$-$P31c$ phase transition. Coefficients e_{11} (squares), e_{33} (triangles), and the volume strain e_v (circles) were calculated after Carpenter et al. (1998).

TABLE 7. Equation of state parameter

Parameter	LPP ($P\bar{6}2c$)	HPP ($P31c$)
V_0 (Å^3)	372.34(4)	376.1(4)
$K_{0,T}$ (GPa)	117.9(7)	88.8(1.6)
a_0 (Å)	6.6387(3)	11.516(4)
K_a (=⅓ β_a^{-1}) (GPa)	108.1(7)	95.4(1.8)
c_0 (Å)	9.7554(4)	9.826(4)
K_c (=⅓ β_c^{-1}) (GPa)	143.3(1.1)	77.2(1.6)

the direction normal to the ring plane, which is defined by the three Si atoms. In three-membered (Si_3O_9) rings with the ideal $\bar{6}2m$ ring symmetry, as in benitoite, γ is 0°, while in $P31c$ the tilt angle γ increases with pressure and the maximum value observed is 7.8° at 6.14 GPa. The normal to the ring plane, which is parallel to the threefold axis in the LPP, is at an angle Γ of 3.3(2)° to the threefold axis at 6.14 GPa. Although maximum values of ca. 25° for γ have been reported for (Si_3O_9)-ring containing structures wollastonite-II, high-pressure $NaYSi_2O_6$, walstromite, and its isostructural compounds (Kahlenberg et al. 2007), tetragermanates related to benitoite display even higher γ values up to 29.7°, and the currently highest known γ-value of 43.6 is found in $BaSiSi_3O_9$, with the ring-normal direction

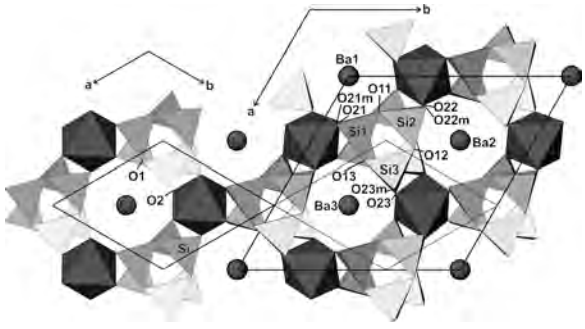

FIGURE 6. Topology of the benitoite structure in a view down the **c**-axis showing the unit cells of the two pressure polymorphs (left: LPP; right: HPP) and the origin shift by [2/3,–2/3,0] relative to setting of the LPP unit cell (=subcell in HPP unit cell, drawn as dotted lines).

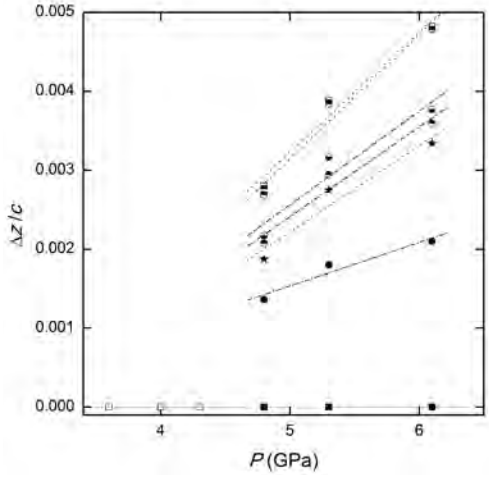

FIGURE 7. Relative shift of the *z*/*c* positional parameter for selected atoms. The shift of the atoms in the HPP phase is given relative to the position of the atom in the LPP phase. Symbols correspond as follows: Ba in LPP = open squares, Ba1 = full squares, Ba2 = squares with full top and open bottom, Ba3 = squares with full bottom and open top, Ti = stars, Si1 = full circles, Si2 = circles with full top and open bottom, Si3 = squares with full bottom and open top.

being 18° off the threefold axis. The increasing inclination of γ in benitoite can be understood by the relatively stronger compression along the **c**-axis, which pushes the Ba atoms more inside the structural channels on one side toward the level of silicate rings. Simultaneously the inter-ring separation decreases considerably, and the displacement of the oxygen atoms is also influenced by the non-bonding interaction between the oxygen atoms between different rings stacked along the **c**-axis direction.

Raman spectra at high pressure

Raman modes and their assignment to vibrational bands in polarized spectra of benitiote have been extensively investigated by Kim et al. (1993) and McKeown et al. (1993). Their study suggests Raman lines associated with eigenmodes of Ba,Ti ring translation and rotation in the low-frequency range (50–300 cm^{-1}), breathing, stretching and deformation modes

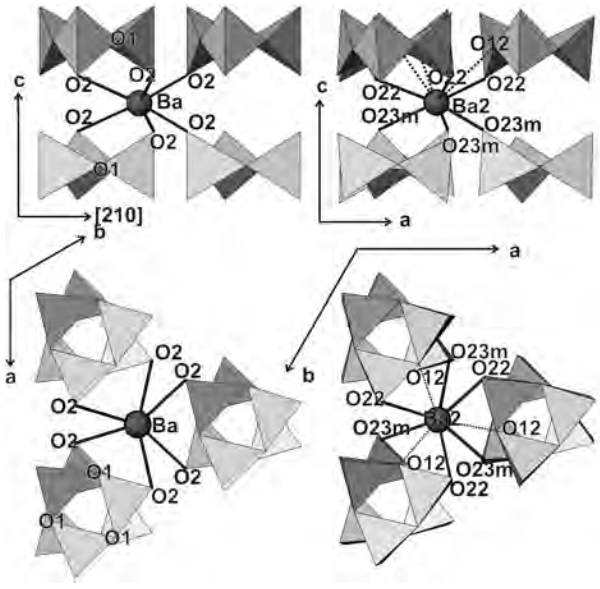

FIGURE 8. Comparison of the stereochemical coordinations of selected barium atoms (Ba of the LPP, Ba2 of the HPP). Views correspond to the **a**-axis (upper row) and **c**-axis (lower row) directions according to LPP base-vector setting.

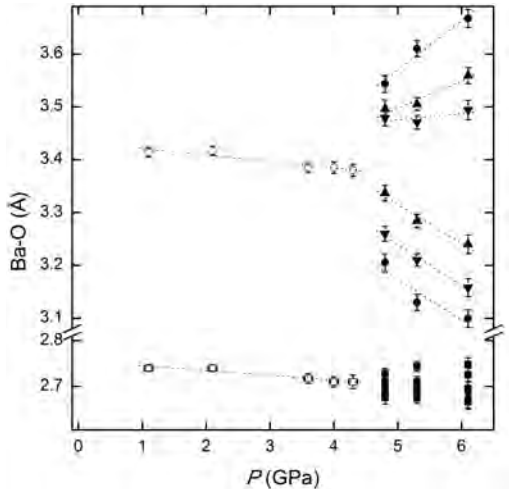

FIGURE 9. Ba-O bond distances as a function of pressure. Open symbols correspond to the LPP (with one Ba site, Ba-O2 = squares, Ba-O3 = circles), closed symbols correspond to the 3 sites in HPP (Ba*i*-O2*i* = squares, Ba1-O1*i* = circles, Ba2-O1*i* = triangles pointing up, Ba3-O1*i* = triangles pointing down).

for the silicate ring in the range 300–800 cm^{-1}, and Si-O bond stretching modes in the frequency range 800–1200 cm^{-1}. Non-polarized Raman spectra of the sample at 1 bar correspond to known spectral features of the calculated and observed modes reported by McKeown et al. (1993).

A series of in total 32 spectra recorded from the two oriented crystals at pressures between 10^{-4} and 9.27 GPa (Fig. 11) reveals very similar spectra across the transition pressure with the position and intensities of the modes being apparently not affected.

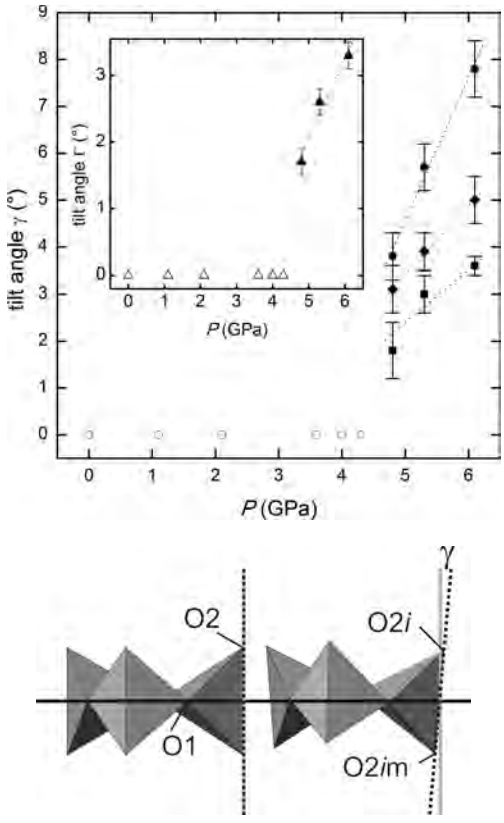

FIGURE 10. (**a**) Tilt angle γ of the SiO_4 tetrahedra with increasing pressure. Symbols correspond as follows: empty symbols for the LPP phase, full symbols for the HPP phase with γ to O21-O21m = diamonds, to O22-O21m = circles, and to O23-O23m = squares. Inlet: Tilt angle Γ of the normal of the plane through the Si_3O_9 rings relative to the **c**-axis direction. (**b**) The tilt angle γ is defined as the angle between the terminal oxygen atoms O2*i* – O2*i*m (*i* = 1,2,3) of each tetrahedron (broken line) and the direction normal to the ring plane (solid line). The ring plane is determined by the baricenters of Si1, Si2, and Si3 atoms. Left: Si_3O_9 ring with $P\bar{6}2m$ symmetry in the LPP phase. Right: Si_3O_9 ring in the HPP form.

The majority of the modes show, as expected, the variation of the band positions with pressure corresponding to a blueshift with $\Delta\nu/\Delta P$ ranging from ~3.3 to ~4.4 cm^{-1} GPa^{-1} (Fig. 12). Out of the most prominent modes only the band assigned as ν_3 reveals a marginally negative shift ($\Delta\nu/\Delta P \approx -1.8$ cm^{-1} GPa^{-1}). The positional shifts are not accompanied by a significant change in the half width (between ~2 and ~5 cm^{-1}), which reflects the ideal hydrostatic conditions on the sample crystals.

The only significant difference between the pattern below and above the transition pressure could be observed for the band ν_{15} loacted at around 1100 cm^{-1} (see Figs. 11 and 12) This band, which has been assigned to a stretching mode of the Si-O1 bond, shows a clear splitting at pressures above the critical transition pressure P_c, with a clear correlation between the degree of splitting and the value for ($P_c - P$). The blueshift $\Delta\nu/\Delta P$ of the two modes in the high-pressure phase is remarkably larger and corresponds to ~16 and ~24 cm^{-1} GPa^{-1}. The differences are

responsible for the increasing line splitting. On the other hand, the single v_{15} band occurring in the spectra below P_c is a very broad band with a half-width of 70 cm^{-1}, which continuously decreases to ~20 cm^{-1} at P_c, while the two individual bands above the transition point are characterized by a more or less constant half-width that ranges between ~6 and ~9 cm^{-1}.

DISCUSSION

From structural point of view the transition being second order in character can be understood from the displacive mechanisms, which originates from the unstable coordination of the barium atoms and the need to adopt the stereochemistry as pressure changes. Atomic displacement could only be achieved by breaking the symmetry-related constraints, i.e., reducing the local site symmetry from 32 to 3, which in turn allows the displacements along the triad relative to the Si_3O_9 ring units. Theoretically possible direct subgroup-group relationship would have suggested $P31c$ (no.159) with a single Ba site, which indeed allows displacement along the z direction, but only by the same amount and vector direction for all Ba atoms. As the cooperative effect of distortion on the Si rings requires individual displacement between adjacent Ba sites, only the reported trigonal supercell provides independent sites of the given local symmetry for a direct group-subgroup-relationship.

It is remarkable that the crystallographic metric corresponding to the supercell has been reported for homologous phases such as the synthetic tetragermanates and -silicates. Synthetic $BaGe(Si,Ge)_3O_9$ solid solution (Goreaud et al. 1973) have shown that if more than 50% of the Si on the tetrahedral position are replaced by germanium, the corresponding solid solutions possess a $P31c$ supercell with $a' = a\sqrt{3}$. Although also pure $BaGeGe_3O_9$ has been described in this supercell setting, the spacegroup was reported to be $P3$ (Robbins et al. 1966) or $P321$ (Smolin 1969). It is worth noticing that all phases, $BaGe(Ge,Si)_3O_9$ in $P31c$ (Goreaud et al. 1973), $BaSiSi_3O_9$ in $P3$ (Hazen et al. 1999), $BaGeGe_3O_9$ in both $P3$ (Robbins et al. 1966) and $P321$ (Smolin 1969) have a different setting with the octahedral position on the origin and only one Ba site. Moreover, the Ba-tetragermanate structure differs from the benitoite structure with respect to the stacking of the tetrahedral layers: there is only one tetrahedral layer per unit cell and hence the Ba-tetragermanate structure reveals $c' = c/2$ in comparison to the benitoite lattice. Moreover, $BaSiSi_3O_9$, one of the rare structures with Si in both four- and sixfold coordination, crystallizes in the Ba-tetragermanate type structure (Hazen et al. 1999). However, it was reported to transform upon grinding or mechanical milling into the benitoite structure (Finger et al.

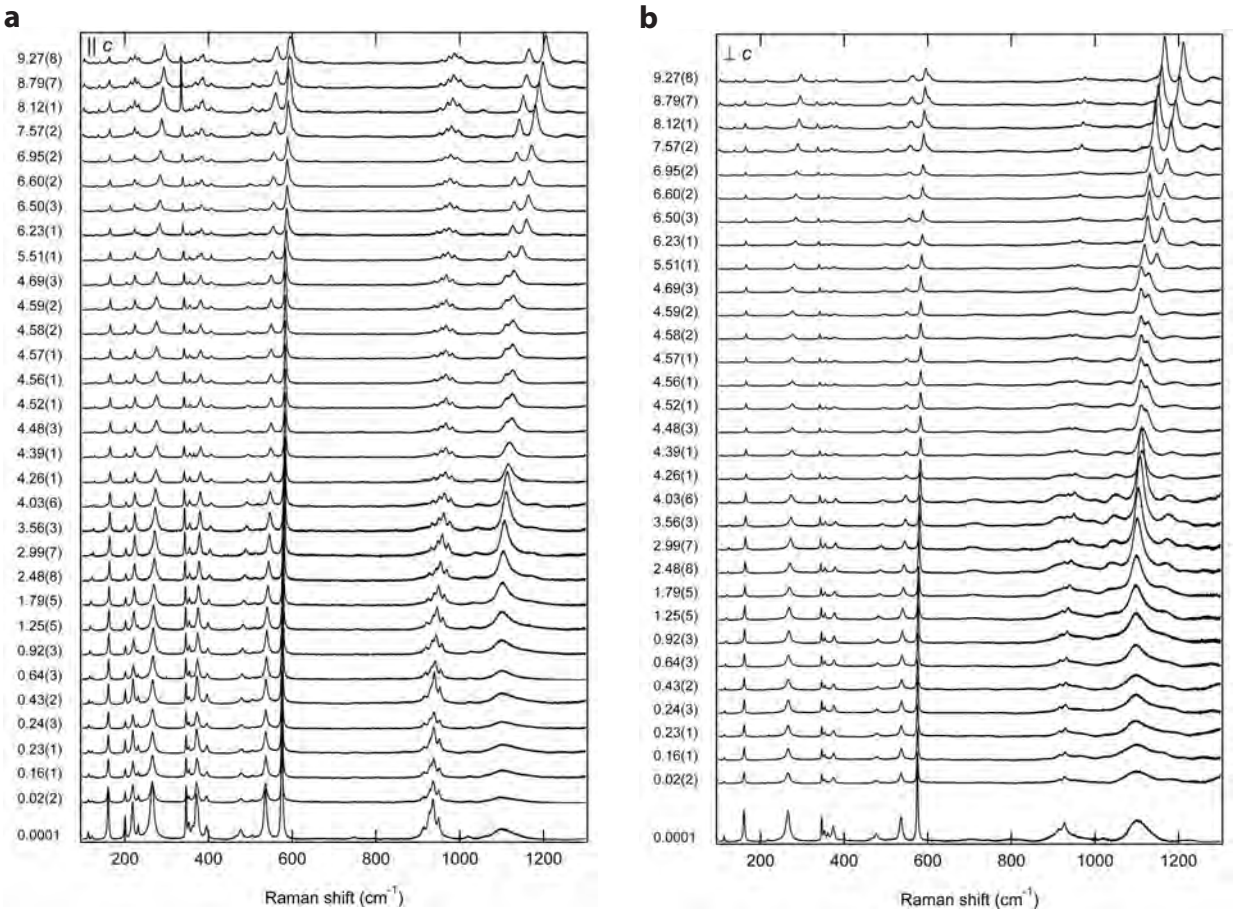

FIGURE 11. Unpolarized in situ high-pressure Raman spectra of oriented benitoite in the spectral range from 100 to 1300 cm^{-1} at pressures between 0.001 and 9.27 GPa: (**a**) spectra for crystal section || **c** and (**b**) spectra for crystal section ⊥ **c**.

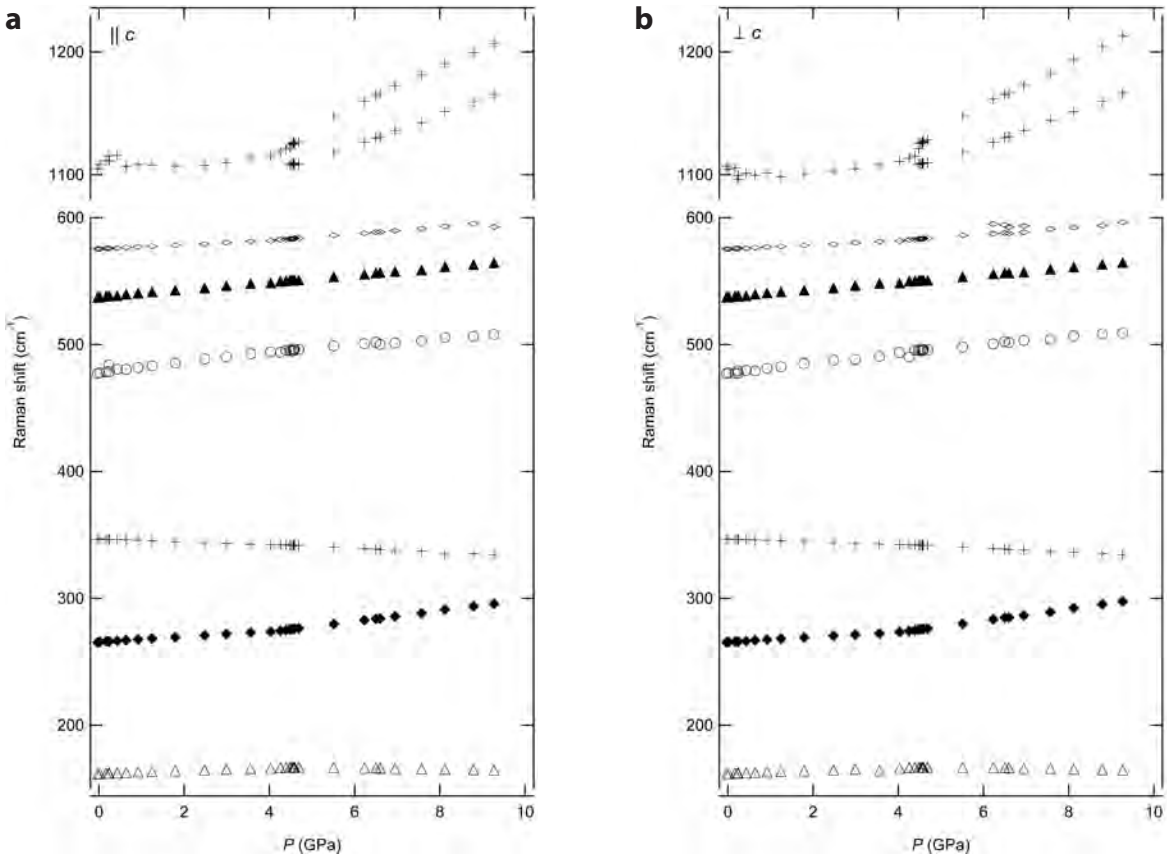

FIGURE 12. Plots of the Raman shift for selected modes (in the spectra || **c** and ⊥ **c**) as a function of pressure (symbols: crosses = ν_{15}, open diamonds = $\nu_2+\nu_4$, closed triangle = ν_6, open circle = ν_{16}; plus = ν_3 closed circle = ν_{13} according to McKeown et al. 1993).

1995; Finger and Hazen 2000).

The common feature of all the above mentioned structures with $a' = a\sqrt{3}$ is that the ring of three tetrahedra gets distorted with deformation of the tetrahedra and loss of the ring symmetry $\bar{6}$ (3/*m*) symmetry. The structural topology of three-membered rings and their distortions resemble the findings observed for equivalent units in several synthetic compounds. In wadeite, $K_2ZrSi_3O_9$ (Henshaw 1955; Blinov et al. 1977), and catapleiite, $Na_2ZrSi_3O_9{\cdot}2H_2O$ (Merlino et al. 2004; Zubkova et al. 2007), the structures possess in analogy to benitoite a framework of ring units and isolated octahedra. However, in the wadeite structure type the connection between the octahedral and the tetrahedral rings is different, as expressed by diverse cavities, which can accommodate larger cations, such as K^+ or Na^+(Blinov et al. 1977).

Following the original intention of this study to track down any structural transformation for the given stereochemical instability around the Ba atoms, the finding of a structural transformation at high pressures is not surprising at all. As coordination changes in general are accompanied in many cases by a sudden volume change around the changing coordination polyhedra, the second-order character observed here for the pressure-induced transformation of benitoite was quite unexpected at first glance. On the other hand, considering that the transition pathway is related to a simple translational displacement of the atoms involved, the solely displacive mechanism allows understanding the lack of any discontinuity, and thus explains the linear fashion of changes with increasing pressure.

From the point of view of crystallographic symmetry, the benitoite structure type is of special interest, because it is the prototype structure for space group $P\bar{6}c2$ (no. 188), a rather rare space group with only 31 representatives in the ICSD (Belsky et al. 2002). Considering group theory, the structures of the two polymorphs of benitoite are in a crystallographic group–subgroup relationship. Actually, the pressure induced transition results in a general subgroup of index six. The relation between the coordinate system of the group G = $P\bar{6}c2$ to that of the subgroup H = $P31c$ can be described by a 3×3 transformation matrix **P** and a column vector **p** representing the origin shift

$$\begin{pmatrix} \mathbf{a}_{HPP} & \mathbf{b}_{HPP} & \mathbf{c}_{HPP} \end{pmatrix} = \begin{pmatrix} \mathbf{a}_{LPP} & \mathbf{b}_{LPP} & \mathbf{c}_{LPP} \end{pmatrix} \times \begin{pmatrix} -1 & -1 & 0 \\ -2 & 1 & 0 \\ 0 & 0 & -1 \end{pmatrix} + \begin{pmatrix} \frac{2}{3} \\ -\frac{2}{3} \\ \frac{1}{2} \end{pmatrix} \quad (1)$$

A more detailed understanding of the phase transformation in benitoite can be achieved by a *symmetry mode analysis*. In the course of this procedure the structural distortions present in a low symmetry structure can be decomposed into contributions from different modes, whose symmetries are given by the *irreducible representations* of the space group of the parent (high-symmetry)

phase (see, for example, Hatch et al. 1987; Kahlenberg 1998; Perez-Mato et al. 2010).

Starting points for the symmetry mode analysis of benitoite were the structures at ambient pressure and at 4.75 GPa as well as the matrix-column pair of the transformation (see above). Figure 13 shows the derived chain of maximal subgroups relating the space group types of the parent and the distorted polymorph. The allowed irreducible distortion components that should be present in the high-pressure phase are also indicated. The onset of a primary mode could directly explain the observed symmetry break with a single transition. It corresponds to the irreducible representation K_6, associated with the point K (⅓,⅓,0) of the first Brillouin zone. However, two secondary modes (Γ_3 and K_5) would be possible as well. These secondary modes are not sufficient for imposing the final distortion symmetry. They do not reduce the symmetry enough by themselves but break the symmetry up to intermediate subgroups. Furthermore, there will be also a trivial fully symmetrical Γ_1 distortion that retains the symmetry of the $P\bar{6}c2$ polymorph. In this scenario one would expect a dominant K_6 distortion component, while the symmetry allowed secondary displacement components should be much weaker. Consequently, the high-pressure form of benitoite would be an improper ferroelectric.

In the next step of mode analyses a basis of symmetry-adopted modes for describing the displacive distortion was obtained performing the mode decomposition of the distortion based on it. A summary of the calculated distortion amplitudes is given in Table 8. It lists the four irreducible representations present in the distortion and the absolute amplitudes of these four symmetry components of the global distortion (last column). As can be seen from the amplitudes, the K_6 mode is significantly larger than the other modes, indicating that the hypothesis of one primary and several secondary distortions is correct. Nevertheless, the K_5 and Γ_1 distortions cannot be neglected for a complete understanding of the distortion pattern.

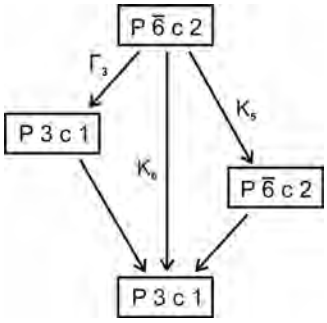

FIGURE 13. Maximal subgroup graph between space groups G = $P\bar{6}c2$ and H = $P31c$. The labels indicate the irreducible distortion components (and the related isotropy subgroups) that can contribute to the symmetry break $P\bar{6}c2 \rightarrow P31c$. The label K corresponds to the wavevector (⅓,⅓,0) in the first Brillouin zone of the low pressure structure of benitoite.

Furthermore, the table gives for each representation its wave vector and the resulting isotropy subgroup.

Finally, for each involved irreducible representation the corresponding *polarization vector* was obtained. Table 9 shows a crystallographic description of these normalized vectors. For the asymmetric unit of the reference structure for each involved irreducible representation the set of correlated atomic displacements (in relative units) is given. The actual distortion of a specific symmetry can be easily obtained by multiplying the components of the polarization vector with the amplitude summarized in Table 8. For K_6 columns 11 to 13 have to be multiplied with an amplitude of 0.6653 Å. From the inspection of Table 9, one can immediately see that the polar Γ_3 distortion component, for example, induces concordant movements of all three Ba atoms. On the other hand, the largest K_6 mode involves an in-phase movement of two Ba atoms (Ba2/Ba3) along **c** as well as an anti-phase displacement of the remaining Ba1, respectively (cf. Fig. 7). There are no components in the x-y-plane. The same principal behavior is observed for the three silicon atoms and the oxygen anions O11-O13. The Ti atoms experience only minor displacements from the K_6 distortion (within the x-y-plane), whereas the oxygen anions O2*i* and O2*i*m (*i* = 1,2,3) have displacement components in all three directions.

TABLE 8. Summary of the mode decomposition of the high-pressure phase of benitoite

Wavevector (Å)	Irrep	Direction	Subgroup	Dimension	Amplitude
(0,0,0)	Γ_1	(a)	$P\bar{6}c2$ (188)	7	0.1393
(0,0,0)	Γ_3	(a)	$P3c1$ (158)	7	0.0721
(⅓,⅓,0)	K_5	(–0.500a,–0.866a)	$P\bar{6}2c$ (190)	16	0.2107
(⅓,⅓,0)	K_6	(0.500a,0.866a)	$P31c$ (159)	12	0.6653

TABLE 9. Normalized polarization vectors of the Γ_1, Γ_3, K_5, and K_6 distortions present in the $P31c$ phase of benitoite expressed as displacements in relative units for the asymmetric unit of the reference structure

	Γ_1			Γ_3			K_5			K_6		
Atom	δx	δy	δz	δx	δy	δz	δx	δy	δz	δx	δy	δz
Ba1	0	0	0	0	0	0.0048	0	0	0	0	0	–0.0262
Ba2	0	0	0	0	0	0.0048	0	0	0.0002	0	0	0.0131
Ba3	0	0	0	0	0	0.0048	0	0	–0.0002	0	0	0.0132
Ti1	0	0	0	0	0	–0.0054	0.0025	0.0025	0	0.0001	–0.0001	0
Si1	0.0069	0.0019	0	0	0	0.0006	0.0066	0.0062	0	0	0	–0.0079
Si2	–0.0019	0.0050	0	0	0	0.0006	–0.0008	–0.0030	0	0	0	0.0031
Si3	–0.0050	–0.0069	0	0	0	0.0006	–0.0025	0.0044	0	0	0	0.0048
O11	–0.0017	–0.0045	0	0	0	–0.0095	–0.0081	–0.0090	0	0	0	0.0120
O12	0.0045	0.0029	0	0	0	–0.0095	–0.0032	0.0150	0	0	0	–0.0009
O13	–0.0029	0.0017	0	0	0	–0.0095	0.0160	0.0101	0	0	0	–0.0111
O21	0.0154	0.0053	0.0001	0.0090	0.0143	0.0046	0.0007	–0.0128	0.0023	0.0070	0.0105	–0.0114
O22	–0.0053	0.0102	0.0001	–0.0143	–0.0053	0.0046	–0.0051	–0.0094	0.0028	0.0031	–0.0050	0.0004
O23	–0.0102	–0.0154	0.0001	0.0053	–0.0090	0.0046	0.0041	–0.0036	–0.0051	–0.0085	–0.0011	0.0110
O21m	0.0154	0.0053	–0.0001	–0.0090	–0.0143	0.0046	0.0007	–0.0128	–0.0023	–0.0070	–0.0105	–0.0114
O22m	–0.0053	0.0102	–0.0001	0.0143	0.0053	0.0046	–0.0051	–0.0094	–0.0028	–0.0031	0.0050	0.0004
O23m	–0.0102	–0.0154	–0.0001	–0.0053	0.0090	0.0046	0.0041	–0.0036	0.0051	0.0085	0.0011	0.0110

ACKNOWLEDGMENTS

We gratefully thank Ilona Fin and Oliver Wienand for their effort in careful preparation of the polished crystal sections, Ilse Glass, Hans-Peter Meyer, and Rainer Altherr for their support to perform and evaluate the EDX analyses, Thomas Pippinger for giving a helping hand with the measurements on the Huber diffractometer. We also thank Beatrice Schuster, GSI Darmstadt, and Lionel Leydet for their help on the Raman spectrometer, which was kindly provided by the Materials Research Group at the GSI Helmholtzzentrum für Schwerionenforschung. We acknowledge the opportunity to carry out powder diffraction measurements via the scope of project HS-3821 at beamline ID27 at the European Synchrotron Radiation Facility, ESRF, Grenoble. Constructive reviews from F. Nestola and D. Allan contributed to improve the manuscript.

REFERENCES CITED

Alfors, J.T., Stinson, M.C., Matthews, R.A., and Pabst, A. (1965) Seven new barium minerals from eastern Fresno County, California. American Mineralogist, 50, 314–340.

Angel, R.J. (2000) Equations of state. In R.M. Hazen and R.T. Downs, Eds., High-Temperature And High-Pressure Crystal Chemistry, 41, p. 35–59. Reviews in Mineralogy and Geochemistry, Mineralogical Society of America, Chantilly, Virginia.

——— (2004) Absorption correction for diamond-anvil pressure cells implemented in the software package Absorb6.0. Journal of Applied Crystallography, 37, 486–492.

——— (2006) Average V2. http://www.rossangel.com

Angel, R.J. and Finger, L.W. (2011) Single: a program to control single-crystal diffractometers. Journal of Applied Crystallography, 44, 247–251.

Angel R.J, Allan, D.R., Miletich, R., and Finger, L.W. (1997) The use of quartz as an internal pressure standard in high-pressure crystallography. Journal of Applied Crystallography, 30, 461–466.

Belsky, A., Hellenbrandt, M., Karen, V.L., and Luksch, P. (2002) New developments in the Inorganic Crystal Structure Database (ICSD): accessibility in support of materials research and design. Acta Crystallographica B, 58, 364–369.

Beran, A. (1974) Das Absorptionsspektrum des Benitoit im nahen Ultrarot. Tschermaks Mineralogische und Petrographische Mitteilungen, 21, 47–51.

Blinov, V.A., Shumyatskaya, N.G., Voronkov, A.A., Ilyukhin V.V., and Belov N.V. (1977) Refinement of crystal-structure of wadeite, $K_2ZrSi_3O_9$, and its relation to kindred structural types. Kristallografiya, 22, 59–65 [in Russian, English translation in Soviet Physics—Crystallography (1977) 22, 31–35].

Carpenter, M.A. and Salje, E.K.H. (1998) Elastic anomalies in minerals due to structural phase transitions. European Journal of Mineralogy, 10, 693–812.

Carpenter, M.A., Salje, E.K.H., and Graeme-Barber, A. (1998) Spontaneous strain as a determinant of thermodynamic properties for phase transitions in minerals. European Journal of Mineralogy, 10, 621–691.

Chervin, J.C., Canny, B., and Mancinelli, M. (2002) Ruby-spheres as pressure gauge for optically transparent high pressure cells. High Pressure Research, 21, 305–314.

Farrugia, L.J. (1999) *WinGX* suite for small-molecule single-crystal crystallography. Journal of Applied Crystallography, 32, 837–838.

Finger, L.W. and Hazen, R.M. (2000) Systematics of high-pressure silicate structures. In R.M. Hazen and R.T. Downs, Eds., High-Temperature And High-Pressure Crystal Chemistry, 41, p. 123–155. Reviews in Mineralogy and Geochemistry, Mineralogical Society of America, Chantilly, Virginia.

Finger, L.W., Hazen, R.M., and Fursenko, B.A. (1995) Refinement of the crystal structure of $BaSi_4O_9$ in the benitoite form. Journal of Physics and Chemistry of Solids, 56, 1389–1393.

Fischer, K. (1969) Verfeinerung der Kristallstruktur von Benitoite $BaTi[Si_3O_9]$. Zeitschrift für Kristallographie, 129, 222–243.

Gaft, M., Nagli, L., Waychunas, G., and Weiss, D. (2004) The nature of blue luminescence from natural benitoite $BaTiSi_3O_9$. Physics and Chemistry of Minerals, 31, 365–373.

Gaft, M., Nagli, L., Waychunas, G., and Panczer, G. (2005) The nature of red luminescence of natural benitoite $BaTiSi_3O_9$. Mineralogy and Petrology, 85, 33–44.

Goreaud, M., Choisnet J., Deschanv, A., and Raveau, B. (1973) Synthesis and structural development of new silicogermanates of benitoite type and related structures. Materials Research Bulletin, 8, 1205–1213.

Hammersley, A.P., Svensson, S.O., Hanfland, M., Fitch, A.N., and Hausermann, D. (1996) Two-dimensional detector software: From real detector to idealised image or two-theta scan. High Pressure Research, 14, 235–248.

Hatch, D.M., Stokes, H.T., and Putnam, R.M. (1987) Symmetry analysis of the microstructure and phase transitions of crystallographic space groups: applications. Physical Review B, 35, 4935–4942.

Hawthorne, F.C. (1987) The crystal-chemistry of the benitoite group minerals and structural relations in (Si_3O_9) ring structures. Neues Jahrbuch für Mineralogie Monatshefte, 16–30.

Hazen, R.M., Yang, H., Finger, L.W., and Fursenko, B.A. (1999) Crystal chemistry of high-pressure $BaSi_4O_9$ in the trigonal (P3) barium tetragermanate structure. American Mineralogist, 84, 987–989.

Henshaw, D.E. (1955) The structure of wadeite. Mineralogical Magazine, 30, 585–595.

Kahlenberg, V. (1998) Symmetry analysis and the atomic distortions of the phase transitions in $CsZnPO_4$. Zeitschrift für Kristallographie, 213, 13–18.

Kahlenberg, V., Konzett, J., and Kaindl, R. (2007) Structural studies on a high-pressure polymorph of $NaYSi_2O_6$. Journal of Solid State Chemistry, 180, 1934–1942.

Kim, C.C., Bell, M.I., and McKeown, D.A. (1993) Vibrational analysis of benitoite $(BaTiSi_3O_9)$ and the Si_3O_9 ring. Physical Review B, 47, 7869–7877.

King, H.E. and Finger, L.W. (1979) Diffracted beam crystal centering and its application to high-pressure crystallography. Journal of Applied Crystallography, 12, 374–378.

Krauss, G., Reifler, H., and Steurer, W. (2005) Conically shaped single-crystalline diamond backing plates for a diamond anvil cell. Review of Scientific Instruments, 76, 105104-1–105104-5.

Laird, J. and Albee, A.L. (1972) Chemical composition and physical, optical, and structural properties of benitoite, neptunite, and joaquinite. American Mineralogist, 57, 85–102.

Larson, A.C. and Von Dreele, R.B. (2000) General Structure Analysis System (GSAS). Los Alamos National Laboratory Report LAUR 86-748.

Louderback, G.D. (1909) Benitoit, ein neuer Edelstein aus Californien. Zeitschrift für Kristallographie, 46, 386–387.

——— (1912) Benitoit, seine Paragenesis und Art des Vorkommens. Zeitschrift für Kristallograohie, 50, 184–185.

Louderback, G.D. and Blasdale, W.C. (1907) Benitoite, a new California gem mineral, with chemical analysis by Walter C. Blasdale, University of California, Department of Geological Science Bulletin, 5, 149–153.

——— (1909) Benitoite, its paragenesis and mode of occurrence, University of California, Departmenty of Geologic Science Bulletin, 5, 331–380.

Ma, C. and Rossman, G.R. (2008) Barioperovskite, $BaTiO_3$, a new mineral from the Benitoite Mine, California. American Mineralogist, 93, 154–157.

Mao, H.K., Xu, J., and Bell, P.M. (1986) Calibration of the ruby pressure gauge to 800-kbar under quasi-hydrostatic conditions. Journal of Geophysical Research—Solid Earth and Planets, 91, 4673–4676.

McKeown, D.A., Bell, M.I., and Kim, C.C. (1993) Raman spectroscopy of silicate rings: Benitoite and the three-membered ring. Physical Review B, 48, 16357–16365.

Merlino, S., Pasero, M., Bellezza, M., Pushcharovsky, D.Yu., Gobetchia, E.R., Zubkova, N.V., and Pekov, I.V. (2004) The crystal structure of calcium catapleiite. Canadian Mineralogist, 42, 1037–1045.

Miletich, R., Reifler, H., and Kunz, M. (1999) The "ETH" diamond-anvil cell design for single-crystal diffraction at non-ambient conditions. Acta Crystallographica, A55: Abstr P08.CC. 001.

Miletich, R., Allan, D.R., and Kuhs, W.F. (2000) High-pressure single-crystal techniques. In R.M. Hazen and R.T. Downs, Eds., High-Temperature And High-Pressure Crystal Chemistry, 41, p. 445–519. Reviews in Mineralogy and Geochemistry, Mineralogical Society of America, Chantilly, Virginia.

Miletich, R., Hejny, C., Krauss, G., and Ullrich, A. (2005) Diffraction techniques: Shedding light on structural changes. In R. Miletich, Ed., Mineral Behaviour at Extreme Conditions, EMU Notes, 7, p. 281–338. Eötvös University Press, Budapest.

Nishi, F. (1996) Strontium tetragermanate, $SrGe_4O_9$. Acta Crystallographica C, 52, 2393–2395.

Orobengoa, D., Capillas, C., Aroyo, M.I., and Perez-Mato, J.M. (2009) AMPLIMODES: symmetry mode analysis on the Bilbao Crystallographic server. Journal of Applied Crystallography, 42, 820–833.

Perez-Mato, J.M., Orobengoa, D., and Aroyo, M.I. (2010) Mode crystallography of distorted structures. Acta Crystallographica A, 66, 558–590.

Periotto, B., Nestola, F., Balic-Zunic, T., Angel, R.J., Miletich, R., and Olsen, L.A. (2011) Comparison between beryllium and diamond-backing plates in diamond-anvil cells: application to single-crystal X-ray diffraction high-pressure data. The Review of Scientific Instruments, 82, 05511-1–05511-5.

Petricek, V., Dusek, M., and Palatinus, L. (2006) Jana2006. The crystallographic computing system. Institute of Physics, Praha, Czech Republic.

Prince, E., Ed. (2006) International Tables for Crystallography Volume C: Mathematical, physical and chemical tables, 3rd ed. Kluwer, Dordrecht.

Robbins, C., Perloff, A., and Block, S. (1966) Crystal structure of $BaGe[Ge_3O_9]$ and its relation to benitoite. Journal of Research of the National Bureau of Standards Section A-Physics and Chemistry, 70A, 385–391.

Rossmann, G.R. (2008) Barioperovskite, a new mineral from the Benitoite Mine, San Benito County, California. Bulletin of the Mineralogical Society of Southern California, 78, 6–11.

Shashkov, A. Yu., Efremov, V.A., Matsichek, I., Rannev, N.V., Venevtsev, Yu.N., and Trunov, V.K. (1981) "The crystal structure of lead alpha-tetragermanate." Zhurnal Neorganicheskoi Khimii' (= Russian Journal of Inorganic Chemistry), 26, 583–587.

Shashkov, A. Yu., Rannev, N.V., and Venevtsev, Yu.N. (1984) Atomic structure of crystals of alpha-$(PbGe_4O_9)$, $BaGe_4O_9$, and $Pb_{2/3}Sr_{1/3}Ge_4O_9$ and features of the coordination of germanium atoms in framework tetragermanates. Koor-

dinatsionnaya Khimiya [= Coordination Chemsitry (USSR)] 10, 1420–1426.
Sheldrick, G.M. (2008) A short history of Shelx. Acta Crystallographica A, 64, 112–122.
Smolin, Y.I. (1969) Crystal structure of barium tetragermanate. Soviet Physics—Doklady, 13, 641–643 (in Russian, English Translation in Doklady Akademii Nauk SSSR, 181, 595–597.
Takahashi, Y., Kitamura, K., Iyi, N., and Inoue, S. (2006) Phase-stability and photoluminescence of BaTi (Si, Ge) O-3(9). Journal of the Ceramic Society of Japan, 114, 313–317.
Toby, B.H. (2001) EXPGUI, a graphical user interface for GSAS. Journal of Applied Crystallography, 34, 210–213.
Tröster, A., Schranz, W., and Miletich, R. (2002) How to couple Landau theory to an equation of state. Physical Review Letters, 88, 055503-1–055503-4.
Ullrich, A., Schranz, W., and Miletich, R. (2009) The nonlinear anomalous lattice elasticity associated with the pressure-induced phase transition in spodumene: A high-precision static compression study. Physics and Chemistry of Minerals, 36, 545–555.
Ullrich, A., Miletich, R., Balic-Zunic, T., Olsen, L., Nestola, F., Wildner, M., and Ohashi, H. (2010) $(Na,Ca)(Ti^{3+},Mg)Si_2O_6$ clinopyroxenes at high pressures: Influence of cation substitution on elasticity and phase transition. Physics and Chemistry of Minerals, 37, 25–43.
Wise, W.S. and Gill, R.H. (1977) Minerals of the benitoite gem mine. Mineralogical Record, 8, 442–452.
Wojdyr, M. (2010) Fityk: a general-purpose peak fitting program. Journal of Applied Crystallography, 43, 1126–1128.
Zachariasen, W. (1930) The crystal structure of benitoite, $BaTiSi_3O_9$. Zeitschrift für Kristallographie, 74, 139–146.
Zubkova, N.V., Pekov, I.V., Turchkova, A.G., Pushcharovskii, D. Yu., Merlino, S., Pasero, M., and Chukanov, N.V. (2007) Crystal structures of potassium-exchanged forms of catapleiite and hilairite. Kristallografiya, 52, 68–72. (in Russian, English translation in Crystallography Reports (2007) 52, 65–70).

Manuscript received March 23, 2012
Manuscript accepted June 19, 2012
Manuscript handled by G. Diego Gatta